MORC2 Mediates Transcriptional Regulation Through Liquid-Liquid Phase Separation and DNA Binding

Yanshen Zhang[1,2,3,#], Yihui Bi[1, 4, #,*],Wenxiu Duan[1,2,#], Weiya Xu[1,2,#], Yu Wei[1,2,3],Wenli Jiang[1,2,3], Feng Zhu[1], Chengdong Huang[1,2,*], Yucai Wang[1,*], and Chao Wang[1,2,3*]

[1]Hefei National Research Center for Physical Sciences at the Microscale, Center for Advanced Interdisciplinary Science and Biomedicine of IHM, Division of Life Sciences and Medicine, University of Science and Technology of China, Hefei, China.

[2]Ministry of Education Key Laboratory for Membraneless Organelles and Cellular Dynamics, Biomedical Sciences and Health Laboratory of Anhui Province, Division of Life Sciences and Medicine, University of Science and Technology of China, Hefei, China.

[3]Department of Neurology, the First Affiliated Hospital of USTC, Division of Life Sciences and Medicine, University of Science and Technology of China, Hefei, China.

[4]Department of Orthopedics, The Second Affiliated Hospital of Anhui Medical University, Hefei, China.

Running title: Multivalent interactions and DNA binding underlies phase separation of MORC2

[#]These authors contributed equally to this work.

[*]Corresponding authors: Yihui Bi (docbyh1992@163.com)

Chengdong Huang (huangcd@ustc.edu.cn);

Yucai Wang (yucaiwang@ustc.edu.cn);

Chao Wang (cwangust@ustc.edu.cn).

Abstract

MORC2 is a chromatin-associated ATPase implicated in transcriptional silencing and human neuropathies such as Charcot–Marie–Tooth disease and spinal muscular atrophy. However, the molecular mechanisms governing its transcriptional regulatory activity remain elusive. Here, we demonstrate that full-length MORC2 undergoes liquid-liquid phase separation (LLPS) to form nuclear condensates, a process essential for transcriptional repression. Endogenous MORC2 forms dynamic condensates in neurons from EGFP-MORC2 knock-in mice, supporting the physiological relevance of LLPS *in vivo*. The 3.1 Å crystal structure of coiled-coil 3 (CC3) reveals a dimeric scaffold that drives phase separation, while multivalent interactions between the intrinsically disordered region (IDR) and a newly defined IDR-binding domain (IBD) further promote condensate formation. Moreover, LLPS enhances MORC2's ATPase activity in a DNA-dependent manner, indicating a functional coupling between phase separation, DNA binding, and enzymatic regulation. RNA-seq analysis shows that only wild-type, but not LLPS-deficient MORC2, represses core target genes in knockout cells, directly linking condensate formation to transcriptional control. Furthermore, disease-associated MORC2 variants alter condensate dynamics, ATPase activity, and DNA binding, offering mechanistic insights into their pathogenic effects. Together, these findings identify LLPS as a key regulatory mechanism for MORC2 function and provide a molecular framework for understanding its role in transcriptional regulation and human disease.

Introduction

Chromatin dynamically regulates DNA accessibility to orchestrate essential processes such as transcription, replication, and DNA repair[1–5]. These processes are dynamically regulated by chromatin-associated complexes, such as the human silencing hub (HUSH) complex[6], which control the accessibility of genetic material to regulatory machinery. The Microrchidia (MORC) protein family, characterized by a conserved N-terminal GHL-ATPase domain and a structurally diverse C-terminal region, regulates gene expression and chromatin organization[7–10]. These C-terminal domains are thought to contribute to dimerization and functional specificity[11–14] (Fig. 1a).

GHL ATPases, including DNA gyrase, Hsp90, and MutL, rely on ATP-dependent dimerization to drive conformational changes essential for substrate engagement and enzymatic regulation[15–19]. Similar mechanisms have been proposed for MORC family members. In humans, the MORC family comprises of five members—MORC1, MORC2, MORC3, MORC4, and SMCHD1, and different MORC paralogs target distinct genomic loci, including transposable elements, viral DNA, and long-exon genes[7,20,21]. The conserved N-terminal GHL-ATPase domain of MORC family proteins has been extensively characterized, implicating the evolutionarily diversified, multi-domain C-terminal regions as key determinants of chromatin targeting and functional specificity. Despite their structural similarities, the molecular basis for MORC-mediated repression remains poorly understood, particularly due to limited structural insight into its full-length and C-terminal regions.

MORC2 has recently been identified as a key regulator of chromatin architecture and gene silencing, primarily through its recruitment to HUSH-target loci via C-terminal CC2 domain-mediated interactions with TASOR and MPP8[12]. While its silencing activity was initially attributed to the N-terminal ATPase domain, genetic complementation studies have revealed that the CW domain and all three coiled-coil (CC) regions are also indispensable for its function[12,13]. Beyond its structured domains, sequence analyses and structural predictions have uncovered an extended intrinsically

disordered region (IDR) spanning the central to C-terminal regions of the protein, suggesting potential regulatory mechanisms beyond enzymatic activity[22].

Transcriptional silencing is often spatially organized within membrane-less nuclear compartments[23,24]. Recent studies suggest that intrinsically disordered regions (IDRs) can drive liquid-liquid phase separation (LLPS), providing a plausible mechanism by which chromatin-associated factors form functional condensates[25,26]. However, the molecular mechanisms driving LLPS in chromatin-associated proteins, and how such phase behavior modulates genome architecture and gene expression, remain poorly defined.

In this study, we provide direct and comprehensive evidence that MORC2 undergoes LLPS to form nuclear condensates. We define the structural basis for this behavior, identifying a dimeric CC3 scaffold and multivalent IDR-IBD interactions as core elements driving phase separation. We further demonstrate that DNA binding promotes LLPS and that phase separation enhances MORC2's enzymatic activity. Using both cellular and *in vivo* models, we establish that LLPS is functionally essential for MORC2-mediated transcriptional repression, offering new mechanistic insights into how LLPS integrates with DNA binding and enzymatic function to regulate gene silencing.

Results

Coiled-coil 3 (CC3) mediates dimerization of full-length MORC2

To determine whether MORC2 has N- and C-terminal dimerization interfaces similar to those in other GHL-type ATPases[27], we established an *in vitro* system to purify full-length (FL) human MORC2 (MORC2FL, residues 1-1032) from HEK293F cells, yielding nucleic acid-free, highly pure proteins for structural and functional analyses (Fig. 1a, b). Analytical size-exclusion chromatography coupled with static light scattering (SLS) demonstrated that MORC2FL forms dimers, with a molecular weight of approximately 239 ± 1 kDa under buffer conditions containing 1000 mM NaCl even in the absence of ATP (Fig. 1c). Notably, the addition of 601 DNA resulted in a detectable increase in molecular weight (303 ± 2 kDa), indicative of DNA-protein complex formation, but did not disrupt the dimeric assembly of MORC2 (Fig. 1c).

To elucidate the atomic structure of MORC2FL, we initially employed negative-stain electron microscopy to reveal that MORC2FL particles were poorly resolved and exhibited considerable heterogeneity. Notably, a subset of particles displayed a morphology consistent with dimer formation (Fig. S1a). To further investigate this, we performed structural prediction of MORC2FL using AlphaFold3 and identified a predicted structure that closely resembled the observed reconstruction (Fig. S1b). We further examined the oligomerization properties of various MORC2 constructs. MORC2ΔCC3-IBD (residues 1-900) was found to exist as a monomer, whereas CC3-IBD (residues 901-1032) and CC3 alone (residues 901-1003) exhibited dimeric properties, confirming the critical role of the CC3 domain in mediating MORC2 dimerization (Fig. 1c, Fig. S1c).

To gain further structural insights, we determined the 3.1 Å crystal structure of the CC3 dimer using X-ray diffraction (Table S1). The structure revealed that the dimer interface is stabilized predominantly by hydrophobic interactions. Three key hydrophobic residues—L911, L915, and F922—form distinct layers within the dimer interface (layers 1-3, Fig. 1e, Fig. S1e, f). The side chains of these residues are buried

within the dimerization interface, creating a hydrophobic core critical for maintaining the stability of the dimer.

We systematically introduced single-point mutations in these hydrophobic residues to assess their contributions to dimerization. SLS analysis demonstrated that the wild-type (WT) MORC2 CC3-IBD (residues 901-1032, with Trx-tag) fragment predominantly exists as a dimer (~61 kDa). In contrast, all three key mutants (L911Q, L915Q, and F922Q) displayed altered molecular weight distributions indicative of disrupted dimer formation and enhanced higher-order oligomerization (Fig. S1g). However, none of these mutations completely disrupted dimerization or converted the dimer to a monomeric state (Fig. S1g). Further analyses of additional single-site mutants (e.g., I908Q, Y921A, F951Q, Y954A, L958Q) showed minimal effects on dimer stability, underscoring the central importance of L915 and its neighboring hydrophobic layers in stabilizing the CC3 dimer (Fig. S1g). Moreover, we examined the dimeric status of truncated CC3 constructs (residues 901-975), which confirmed that the CC3 domain alone is sufficient to drive dimer formation (Fig. 1f). To delineate the structural basis of these interactions, we mapped the positions of hydrophobic residues within the CC3 backbone (Fig. S1e). The distances between interacting residues, such as I908-I908' (3.4 Å), L911-L915' (3.7 Å), F922-F922' (3.9 Å), and L958-L958' (4.0 Å), revealed a tightly packed hydrophobic network. The robustness of this network ensures the integrity of the CC3 dimer, even under varying physiological conditions. These findings collectively suggest that the CC3 domain plays a critical role in MORC2 dimerization. The dimeric assembly of CC3 is essential for maintaining the structural integrity of the protein, which likely underpins its functional activities, including interactions with chromatin.

MORC2 forms condensates both *in vivo* and *in vitro*

In the predicted structure of MORC2FL, we noticed a long unstructured region at its C-terminus (Fig. S1b), a characteristic often associated with proteins capable of phase separation[25]. To further investigate this, we utilized the IUPred2A tool to predict disordered regions in MORC2FL. The analysis revealed that the previously

undefined 593-735 region predominantly exhibits disorder, prompting us to classify it as an intrinsically disordered region (IDR) (Fig. 1a).

Next, we explored whether MORC2FL exhibits phase separation properties. Lowering the salt concentration to physiological levels is a common strategy for inducing LLPS[28]. Sedimentation assays showed that when the salt concentration was reduced to 150 mM, more than half of the EGFP fused MORC2FL (EGFP-MORC2FL) precipitated into the pellet fraction (Fig. 2a, b). Fluorescence imaging revealed that at a salt concentration of 150 mM, EGFP-MORC2FL spontaneously demixed to form well-defined spherical droplets of varying sizes, which increased in size with rising protein concentration (Fig. 2c, d, and Fig. S2a). Sedimentation assays further showed that the pellet fraction of EGFP-MORC2FL after centrifugation was concentration-dependent (Fig. S2b). The EGFP-MORC2FL-enriched condensates exhibited dynamic behavior, including droplet fusion (Fig. S2c) and fluorescence recovery after photobleaching (FRAP) (Fig. 2e, f), indicating a liquid-like state.

Using antibody labeling, we observed that endogenous MORC2 forms dense punctate structures in the nucleus of HeLa cells (Fig. 2g), whereas these structures are absent in MORC2-knockout HeLa cells (Fig. S2d, e), suggesting that MORC2 may undergo LLPS in the nucleus. To further investigate this, we transfected HeLa cells with EGFP-MORC2FL and observed that EGFP-MORC2FL formed dense, droplet-like condensates in the nucleus (Fig. 2h). Notably, in agreement with antibody staining results, EGFP-MORC2FL condensates preferentially localize to regions of reduced chromatin density, as indicated by histone H2A-mCherry signal. This spatial distribution suggests a potential role for MORC2 condensates in heterochromatin regulation. FRAP of EGFP-MORC2FL puncta revealed recovery on the timescale of seconds in these transfected HeLa cells (Fig. 2i, j), consistent with characteristics of liquid-like condensates with a highly dynamic internal environment.

To determine whether MORC2 forms phase-separated biomolecular condensates under physiological conditions, we generated mice expressing EGFP-MORC2 protein from the endogenous locus (Fig. S2f). We focus on neurons in brain and spinal cord as

missense mutations in *MORC2* cause neuropathies including Charcot-Marie-Tooth and spinal muscular atrophy disease[11,13]. Imaging of NeuN-positive neurons revealed that EGFP-MORC2FL condensates occur in neurons under endogenous expression level (Fig. 2k). FRAP analysis in freshly prepared brain slices further demonstrated rapid and partial fluorescence recovery, supporting the dynamic and liquid-like nature of endogenous MORC2 assemblies (Fig. 2l). In addition, unlike MORC3, which shows cell cycle-dependent nuclear puncta formation[29], MORC2 condensates were absent in mitotic cells (Fig. S2g). Together, these results indicate that MORC2 forms phase-separated biomolecular condensates under physiological conditions *in vivo*.

The MORC2 C-terminal domain (CTD) drives condensate formation

To identify the key determinants of MORC2 LLPS, we divided the protein into two distinct domains: the N-terminal domain (NTD, residues 1-472), which includes the ATPase and CC1 domains, and the C-terminal domain (CTD, residues 473-1032), containing the IDR. A series of EGFP-tagged truncation constructs were expressed in HeLa cells (Fig. 3a). Deletion of the CTD disrupted puncta formation and resulted in diffuse localization across the nucleus and cytoplasm (Fig. 3a, Fig. S3a). By contrast, NTD deletion had little effect on nuclear localization or condensate formation (Fig. 3a, Fig. S3a). Addition of an exogenous nuclear localization signal (PKKKRKV)[30] to the NTD redirected it to the nucleus but failed to restore puncta formation (Fig. 3a), indicating that the CTD is necessary for condensate assembly.

Further dissection of the CTD revealed that deletion of either the CC2 or TCD domains did not impair its ability to form nuclear puncta (Fig. S3b). In contrast, removal of the IDR-NLS region (residues 593-761) disrupted both puncta formation and nuclear localization (Fig. S3b). Notably, even when nuclear localization was restored by fusing the PKKKRKV to CTDΔIDR-NLS, puncta formation remained abolished (Fig. S3c), indicating that the IDR is essential for condensate formation. Deletion of the CC3-IBD segment allowed nuclear localization but also abolished puncta formation, suggesting that this region is likewise required (Fig. S3b). However, neither the IDR-NLS fragment alone, the CC3-IBD fragment alone, nor the

PKKKRKV-fused CC3-IBD fragment was sufficient to form puncta (Fig. S3d), implying a cooperative role between these two regions. The CW domain modulates condensate size, as its deletion led to enlarged and often fused CTDΔCW puncta. In the context of MORC2FL, we final conclude that the IDR, CC3, and IBD constitute the structural core required for condensate formation, while the CW domain restricts condensate overgrowth or fusion (Fig. 3a, Fig. S3e). Notably, condensates formed exclusively in the nucleus and not in the cytoplasm of transfected HeLa cells, suggesting that chromatin-associated nuclear factors, such as DNA, may contribute to the nucleation or stabilization of MORC2 condensates.

To assess whether the CTD is intrinsically prone to LLPS *in vitro*, we expressed and purified CTDΔCW from *E. coli*, as the CTD exhibited poor biochemical stability (Fig. S4a, b). Under 150 mM NaCl conditions, Cy3-labeled CTDΔCW readily formed condensates in a concentration-dependent manner (Fig. 3b, c), and underwent phase separation-associated sedimentation (Fig. 3d, e). Fluorescence microscopy and static light scattering (SLS) confirmed that Cy3 labeling did not affect its phase behavior, droplet morphology, or molecular weight distribution (Fig. S4c–f).

Multivalent interactions between IDR and CC3-IBD promote MORC2 LLPS

Next, we elucidated the mechanistic basis for MORC2 phase separation mediated by the IDR and residues CC3-IBD. We hypothesized that multivalent interactions likely exist between the IDR and CC3-IBD, which are important for driving LLPS, leading to a condensed phase coexisting with a dilute aqueous phase. Using nuclear magnetic resonance (NMR) spectroscopy, we investigated the interaction between the IDR and the CC3-IBD fragment (Fig. 4a-c). The ^{15}N-labeled CC3 (residues 901-1003) or IBD (residues 1004-1032) samples were prepared for ^{15}N-HSQC assays. Titration experiments with the IDR (residues 593-735) revealed that the IBD is the primary binding site, whereas the CC3 region showed minimal interaction (Fig. 4b, c). Sequence analysis confirmed that IBD is enriched in acidic residues and is highly conserved across species, which may facilitate its interaction

with the basic residues in the IDR (Fig. 4g). Further subdivision of the IDR into three segments—IDRa (residues 593-643), IDRb (residues 644-694), and IDRc (residues 695-735)—pinpointed IDRa as the key region responsible for interaction with IBD (Fig. 4a, d-f). NMR titration data indicate that IDRa binds IBD via transient weak interactions (Fig. 4d, g). The partial compaction of IDRa, which we identify as a proline-arginine-rich region, together with its weak multivalent association with IBD (Fig. 4g), may serve as a nucleation mechanism for LLPS—an organizational strategy that has also been observed in other phase-separating proteins[31–33].

To assess the role of IDRa-IBD multivalent interactions in promoting MORC2 LLPS within the nucleus, we transfected full-length MORC2 constructs with individual deletions of the IBD, IDRa, IDRb, or IDRc regions. Deletion of the IBD markedly reduced droplet formation in both HeLa cells (Fig. 3a, Fig. S3e) and HEK293T cells (Fig. S5). Similarly, deletion of IDRa significantly reduced condensate formation, resulting in a marked decrease in both droplet area and size (Fig. 4h, i). In contrast, deletion of IDRb or IDRc had minimal impact on droplet formation (Fig. 4h, i). Based on these findings, we propose a model in which multivalent interactions between the IDRa and IBD drive MORC2 intermolecular assembly, a process further potentiated by CC3-mediated dimerization, which is essential for LLPS (Fig. 4j).

DNA binding promotes MORC2 phase separation and ATPase activity

Our results indicate that nuclear localization is critical for MORC2 condensate formation when over-expressed in HeLa cells. As MORC2 has been reported to bind DNA via its CC1 domain[13], we further assess the role of DNA binding in regulating its LLPS behavior. To this end, we first purified MORC2FL and several truncated variants, and assessed their ability to bind 601 DNA using electrophoretic mobility shift assays (EMSA). Increasing concentrations of MORC2FL progressively retarded 601 DNA migration, confirming direct DNA binding (Fig. 5a). Consistent with previous reports[13], CC1-containing constructs exhibited robust DNA-binding activity (Fig. 5b). Notably, the CC2 and IDR domain also displayed strong DNA-binding

activity (Fig. 5c, d). In addition, while the CC3-IBD fragment showed no detectable effect on 601 DNA migration (Fig. 5f), the TCD-CC3-IBD construct clearly impaired migration (Fig. 5e), indicating that the TCD also possesses DNA-binding capability.

Building on these findings, we tested whether DNA enhances MORC2 LLPS *in vitro*. At 0.9 μM, MORC2FL alone failed to form droplets; however, the addition of 25 nM 601 DNA induced robust condensate formation, indicating that DNA promotes MORC2 phase separation (Fig. 5g, h). Moreover, 601 DNA also facilitated droplet formation by the CTDΔCW construct (Fig. 5i). Together with the observation that the TCD is dispensable for condensate formation and that the CC3-IBD fragment does not bind DNA, these results suggest that DNA-induced condensation is primarily mediated through interactions with the IDR-NLS region. We speculated that this interaction is driven by nonspecific electrostatic attraction between DNA and the arginine/lysine-rich sequence within the IDR-NLS (Fig. 4g).

We further examined the impact of DNA binding on MORC2 ATPase activity. The presence of 601 DNA markedly enhanced ATP hydrolysis, indicating that DNA binding positively modulates MORC2 enzymatic function (Fig. 5j). To confirm that the observed activity is intrinsic to MORC2, we included the ATP-binding-deficient mutant N39A as a negative control. N39A exhibited negligible ATP hydrolysis under both basal and DNA-stimulated conditions, in contrast to the robust and DNA-enhanced activity observed with the WT protein (Fig. 5j). Together, these findings reveal a synergistic interplay between phase separation, DNA binding, and ATPase activity, highlighting their collective importance in coordinating transcriptional regulation.

LLPS is required for MORC2-mediated transcriptional repression

To evaluate whether phase separation contributes to MORC2-dependent transcriptional regulation, we performed rescue experiments in MORC2-knockout HeLa cells by expressing EGFP, EGFP-MORC2FL, EGFP-MORC2ΔCC3, or EGFP-MORC2ΔIDR, respectively. Bulk RNA sequencing was used to assess transcriptomic changes induced by FL MORC2 and LLPS-deficient mutants (Fig. 6a).

Expression analysis confirmed robust overexpression of EGFP-MORC2FL and EGFP-MORC2ΔCC3 compared to EGFP controls (424.9-fold and 542.7-fold increases, respectively), while EGFP-MORC2ΔIDR exhibited only a 2.2-fold increase (Fig. 6b). Given that transfection conditions were identical and that this low expression was consistently observed across three replicates, we speculate that IDR deletion may impair mRNA stability or transcription. Accordingly, the EGFP-MORC2ΔIDR group was excluded from downstream analyses.

Relative to EGFP, re-expression of EGFP-MORC2FL led to differential expression of 240 genes (fold change > 1.2 or < 0.83, $p < 0.05$), including 182 downregulated and 58 upregulated transcripts (Fig. S6a). Gene Ontology (GO) analysis showed that these genes are primarily localized to nucleus and chromatin compartments (Fig. S6b), and enriched for functions related to transcriptional regulation (Fig. S6c), including DNA-binding transcription factors and cytokine genes (Fig. S6d). These results are consistent with MORC2's known role in transcriptional silencing.

The LLPS-deficient MORC2ΔCC3 mutant showed markedly reduced regulatory capacity on these targets (Fig. S6a, e). Notably, among 21 high-confidence MORC2 target genes previously reported in the literature (Fig. 6c), including 18 repressed and 3 activated genes (Fig. 6d), MORC2ΔCC3 failed to repress any of the 18 downregulated targets, while its effect on the upregulated genes was modest (Fig. 6e, f). These findings indicate that condensate formation is essential for the transcriptional repression activity of MORC2. Together, these results support a model in which phase separation underpins MORC2's transcriptional regulatory function by enabling its engagement with chromatin-associated gene silencing pathways.

Pathogenic MORC2 variants differentially affect phase separation, DNA binding, and ATPase activity

MORC2 is essential for gene silencing at H3K9me3-marked loci, chromatin regulation, and retrotransposon repression[6,34–36]. Pathogenic mutations in its GHL-type ATPase domain have been associated with neuropathies and cancer[37–41].

We examined a panel of disease-associated variants, including those linked to Charcot–Marie–Tooth disease type 2Z (CMT2Z: E236G, R252W, Q400R, D466N, colored in red) and spinal muscular atrophy (SMA: S87L, S218L, F256L, R266A, T424R, colored in blue) (Fig. 7a). In HeLa cells transiently expressing these variants, none disrupted nuclear condensate formation, likely due to their localization within the N-terminal ATPase domain (Fig. 7b). However, the CMT2Z-linked E236G and the SMA-linked T424R mutants led to a significantly higher proportion of cells exhibiting nuclear condensates, suggesting these mutations promote MORC2 phase separation (Fig. 7b). *In vitro* ATPase assays revealed that T424R significantly increases enzymatic activity (Fig. 7c), consistent with its reported role in promoting ATPase dimer cycling[13]. Additionally, S218L and F256L variants also enhanced ATP hydrolysis, whereas others, such as Q400R and D466N, showed activity comparable to WT (Fig. 7c). Due to severe solubility issues, E236G could not be biochemically characterized *in vitro*.

We next assessed DNA binding affinity of MORC2 variants using fluorescence polarization (FP) assays. Despite subtle differences among the variants, none significantly altered DNA-binding capacity compared to wild-type MORC2 (Fig. 7d), indicating that the disease-associated mutations primarily affect enzymatic and phase behaviors rather than DNA affinity. Taken together, these results highlight the functional plasticity of MORC2's N-terminal domain in modulating enzymatic activity and phase separation, while reinforcing the role of LLPS as a regulatory mechanism rather than a prerequisite for DNA binding. These findings also provide mechanistic insight into how specific mutations may contribute to distinct pathological outcomes.

In summary, our results support a model in which MORC2 enforces transcriptional silencing via multivalent interactions that promote liquid–liquid phase separation. The N-terminal ATPase domain undergoes conformational cycling between open and closed states, while the C-terminal CC3-mediated dimer acts as a stable scaffold for condensate formation (Fig. 7e). Electrostatic interactions between the basic regions of MORC2 and chromosomal DNA further potentiate phase

separation and ATPase activation. Together, these properties enable MORC2 to bridge distal chromatin regions and establish repressive condensates, highlighting its central role in chromatin organization and genome stability.

Discussion

Our integrative structural and functional analyses uncover a direct, mechanistically validated role for MORC2 phase separation in gene regulation, extending the understanding of chromatin-associated ATPases. The MORC gene family is evolutionarily conserved and plays a central role in epigenetic regulation and genome stability[42–44]. Originally identified in mice, MORC proteins are crucial for spermatid formation and meiotic progression[45,46]. Human MORC proteins share a characteristic domain architecture, but the mechanisms governing their chromatin interactions, especially in their full-length forms, remains unknown owing to the lack of comprehensive structural information.

In this study, we provide evidence that MORC2 undergoes liquid-liquid phase separation (LLPS) both *in vivo* and in *vitro*, forming dynamic nuclear condensates and driven by multivalent interactions between its IDR and IBD domain, and scaffolded by CC3-mediated dimerization. We demonstrate that full-length MORC2, along with its C-terminal domain, forms LLPS droplets exhibiting key characteristics, including salt sensitivity and recovery after photobleaching. Moreover, nucleosome assembly 601 DNA enhances condensate formation. Importantly, we demonstrate that LLPS is essential for the transcriptional repression activity of MORC2, and phase separation-deficient variants of MORC2 markedly reduce its silencing capacity. Notably, under our ATPase assay conditions, several disease-associated MORC2 variants—particularly S218L, F256L, and T424R—exhibited elevated enzymatic activity compared to WT. This trend partially aligns with previous findings for T424R, but differs from reports describing S87L as a loss-of-function mutant. We speculate that differences in ionic strength and assay sensitivity, as well as potential LLPS-mediated local enrichment of MORC2, may contribute to this discrepancy. These results highlight the importance of biophysical context in interpreting the functional consequences of disease mutations and warrant further mechanistic investigation. Together, our findings uncover a previously unrecognized LLPS-based mechanism by which MORC2 regulates chromatin transcriptional activity, and

suggest a potential connection between this process and neurodevelopmental pathology.

Mutations in human MORC proteins have been linked to diverse pathologies, including inflammatory and neurodevelopmental disorders, as well as cancer[47–49]. MORC2, in particular, has been implicated in the repression of transgenes at H3K9me3-enriched loci and in chromatin relaxation following DNA damage[5,12,50]. Missense mutations within its ATPase domain are causally associated with axonal neuropathies, underscoring the functional importance of ATP hydrolysis *in vivo*. ATP-dependent dimerization of the MORC2 ATPase domain is essential for its transcriptional regulatory activity. In addition, MORC2 contributes to the silencing of retrotransposons and specific gene classes, including LINE-1 elements and intronless genes, highlighting its broader role in maintaining genome integrity[51,52]. The silencing function of MORC2 requires its ATPase activity and its three coiled-coil domains. While the CW and TCD domains are potential chromatin-binding regions, only the CC1 domain is known to bind DNA. Our findings in this study further reveal that the intrinsically disordered region (IDR) of MORC2 exhibits strong DNA-binding capacity, providing new insights into the regulatory mechanisms of MORC2, emphasized the role of arginine/lysine-rich disordered regions in facilitating electrostatic DNA binding[53–56]. These findings refine our understanding of MORC2's function in chromatin architecture and illuminate its mechanistic involvement in human disease.

In conclusion, this study demonstrates that MORC2 undergoes liquid–liquid phase separation to form nuclear condensates, regulated by DNA binding and associated with chromatin condensation and transcriptional silencing. The interplay between phase separation and ATPase activity in MORC2 reveals a distinct mechanism of transcriptional repression. These insights enhance our understanding of MORC2's molecular mechanisms and lay the groundwork for further studies on its role in human diseases.

Materials and Methods

Plasmid construction, cell culture and transfection

WT MORC2 (UniProt: Q9Y6X9) cDNA was amplified from a cDNA library derived from HeLa cells via reverse transcription. The MORC2 cDNA was then subcloned into the p3xFLAG-Myc-CMV-24 vector between BglII and KpnI restriction sites using seamless cloning. The seamless cloning process was facilitated by the ClonExpress II One-Step Cloning Kit (Vazyme, #C112-02) according to the manufacturer's instructions. An EGFP sequence was subsequently inserted into the BglII site at the N-terminal of MORC2 to generate the EGFP-MORC2 construct. To generate deletion mutant constructs of MORC2 for intracellular studies, specific regions of MORC2 were targeted and deleted using a polymerase chain reaction (PCR)-based approach. An 18- or 21 bp homologous sequence originating from one of the forward or reverse primers was introduced into the other primer, and the resulting PCR products were subjected to homologous recombination cloning, facilitated by the 18-bp homologous sequence. For protein expression and purification, MORC2FL and truncated MORC2 were cloned into prokaryotic expression vectors with MBP or Trx fusion proteins for bacterial expression. In addition, MORC2FL and a series of truncation mutants were purified using a HEK293F eukaryotic expression system for *in vitro* phase separation and static light scattering (SLS) assays. Detailed information on all protein purifications and their experimental applications in this study is provided in Table S2. HeLa, HEK293T cells were cultured in DMEM medium (Biological Industries, DMEM, high re maintained in a humidified incubator at 37 °C with 5% CO_2. Cell transfection was performed using Lipofectamine 3000 (Invitrogen) according to the manufacturer's instructions. Briefly, cells were seeded in appropriate culture plates the day before transfection and allowed to reach 40-60% confluency. The separately diluted Lipofectamine 3000 reagent and plasmids in Opti-MEM reduced serum medium (Gibco) were mixed, and the transfection complexes were added to cells after 20 minutes. After a 6-hour incubation, the transfection medium was replaced with fresh complete DMEM medium.

Recombinant protein expression, purification

Plasmids containing His-tagged genes were transformed into *E. coli* BL21 (DE3) cells and cultured in Luria-Bertani medium with 50 mg/L ampicillin. When the culture reached an optical density (OD) of 0.6-0.8 at 600 nm, the temperature was lowered to 16 °C. Isopropyl β-D-1-thiogalactopyranoside (IPTG) (0.25 mM) was added to induce protein expression for 18-20 hours. Cells were harvested by centrifugation at 13,000 × g for 15 minutes, then resuspended in Buffer A (50 mM Tris-HCl, pH 8.0, 1000 mM NaCl, 10 mM imidazole, 1 mM dithiothreitol (DTT), and 1 mM phenylmethylsulfonyl fluoride (PMSF)). The cell suspension was snap-frozen and stored at −80 °C for subsequent protein purification. HEK293F suspension-adapted cells were cultured in conical flasks at 37 °C, 120 rpm, and 5% CO_2, until a density of 1.0×10^6 cells/mL was reached. The cells were transiently transfected with 1 mg of MORC2-6 × His plasmid using 2 mL of branched polyethyleneimine (1 mg/mL). After 48 hours of incubation, cells were harvested by centrifugation at 3,000 × g for 5 minutes, resuspended in Buffer A, snap-frozen, and stored at −80 °C for further purification.

All purification steps were performed at 4°C to preserve protein activity. Frozen cell suspensions were rapidly thawed in water, lysed by sonication (200 W for ~0.3 hours), and centrifuged at 20,000 × g for 30 minutes at 4 °C. The supernatant was filtered through a 0.22 μm syringe filter to obtain soluble material. A His-Trap Ni-NTA 6FF chromatography column was equilibrated with five column volumes of Buffer A (Buffer A: 50 mM Tris-HCl, pH 8.0, 1000 mM NaCl). The clarified extract was loaded onto the column, washed with Buffer A to remove non-specific proteins, and eluted with a linear gradient of nickel elution buffer (Buffer B: 50 mM Tris-HCl, pH 8.0, 1 M NaCl, 300 mM imidazole, 1 mM DTT). Eluted fractions were analyzed by SDS-PAGE and Coomassie staining. The protein of interest was concentrated, exchanged into Buffer C (50 mM Tris-HCl, pH 8.0, 1000 mM NaCl, 1 mM EDTA, 1 mM DTT) using an Amicon Ultra centrifugal filter unit, following overnight treatment with Benzonase nuclease to eliminate nucleic acid contamination or HRV

3C Protease to cut His-tag. The purification process was subsequently refined through gel filtration using a Superdex 6 Increase column (GE Healthcare) for the MORC2FL. Following this, fragments were conjugated with a GPGS linker, and the resulting mixture was subjected to a size-exclusion chromatography process (Superdex 200/75 column, GE Healthcare) to yield a final solution comprising 50 mM Tris-HCl, pH 8.0, 500 mM NaCl, 1 mM EDTA, and 1 mM DTT. Peak fractions were analyzed by SDS-PAGE and Coomassie staining, confirming the successful purification of highly homogeneous MORC2FL (1-1032) and various fragments (Fig. S7), then flash-frozen in liquid nitrogen and stored at −80 °C.

Crystallization, data collection and processing

The CC3 domain (901-1003) and various mutations of MORC2constructs were cloned into a modified pET32M vector (with Trx-tag) using standard PCR-based methods and confirmed by DNA sequencing. Due to the lack of homologous structures, protein crystals with heavy atom derivatives are required to determine their phases. Therefore, we used the methionine-deficient strain B834 to express the target protein with selenomethionine (SeMet) in an inorganic selenosubstituted medium. Recombinant proteins were expressed in *E. coli* B834 cells in M9 medium at 16 °C. MORC2 CC3 fused with a GPGS linker were finally changed by step of size-exclusion chromatography (Superdex 75 increase column, GE Healthcare) into 50 mM Tris-HCl, pH 8.0, 100 mM NaCl, 1 mM EDTA and 1 mM DTT). The freshly purified protein was concentrated to 10~20 mg/mL. Crystals were obtained by the static sitting drop method in 0.1M Citric acid (pH 3.5) and 25% w/v PEG 3350 at 25°C. Glycerol (20%) was added as the cryo-protectant. A 3.1-Å resolution X-ray dataset was collected at the beamline BL18U1 of the Shanghai Synchrotron Radiation Facility (SSRF). The diffraction data were processed and scaled by HKL2000 (http://www.hkl-xray.com/). Using the structure of auto-build model by SAD data and AlpahFold2 predicted model as the search model, the initial structural model was solved by molecular replacement in PHASER (https://www.ccp4.ac.uk/). Further manual model adjustment and refinement were completed iteratively using COOT and

PHENIX. The final structure was validated by PISA and MolProbity (https://www.phenix-online.org/). The final refinement statistics of the complex structure are listed in Supplementary Table 1. All structure figures were prepared using the programme PyMOL (http://pymol.sourceforge.net/).

Protein labeling with fluorophore

The Cy3 NHS ester (AAT Bioquest) fluorophores were dissolved in DMSO at 10 mg/mL. Purified proteins were prepared in reaction buffer at a concentration of 10 mg/mL. The fluorophores were added to the protein solution at a 1:1 molar ratio. The reaction was conducted with shaking at room temperature for 1 hour in the dark. After the reaction, labeling was quenched with 200 mM Tris-HCl, pH 8.3, and the labeled proteins were desalted using a HiTrap desalting column (GE Healthcare). Fluorescence labeling efficiency was assessed using a Nanodrop 2000 spectrophotometer (ThermoFisher #ND-2000). The final labeling efficiency of each protein was adjusted to 1% by mixing the labeled protein with an excess of unlabeled protein (1:99 ratio).

Lentiviral mediated H2A-mCherry inducible expression in HeLa cells

Stable expression of H2A-mCherry in HeLa cells was achieved through lentiviral-mediated transduction. First, H2A-mCherry gene sequence was inserted into the inducible lentiviral vector pTRIPZ to generate the expression plasmid pTRIPZ-H2A-mCherry. Lentiviral particles were generated by triple transfection of HEK293T cells with pTRIPZ-H2A-mCherry, PMD2.G, and PSPAX2 plasmids using Lipofectamine 3000. The viral supernatant was collected 48 hours after transfection, filtered with 0.45-μm filter to remove cell debris, and used to transduce HeLa cells. Following transduction, HeLa cells were selected with 50 μg/mL hygromycin to establish stable cell lines. H2A-mCherry expression was induced with 1 μg/mL doxycycline.

Live cell imaging and immunofluorescence staining

For live-cell imaging, HeLa cells were seeded onto 35 mm culture dishes with glass-bottom plates (Biosharp) and transfected with EGFP-MORC2 or its mutant constructs. Images were captured 12 hours post-transfection using a Nikon confocal microscope equipped with an incubator system (37 °C, 5% CO_2). Nuclei were stained with Hoechst 33342 or visualized using mCherry-labeled H2A fusion protein. For immunofluorescence, cells were fixed with 4% paraformaldehyde, permeabilized with 0.1% Triton X-100, and blocked with 10% goat serum. Primary antibodies were incubated overnight at 4 °C, followed by incubation with fluorescence-conjugated secondary antibodies for 2 hours at room temperature in the dark. Fluorescence images were acquired using a Nikon confocal microscope.

CRISPR-Cas9 mediated MORC2 knockout cells

MORC2 knockout (KO) HeLa cell lines were generated using the CRISPR-Cas9 system. A CRISPR single-guide RNA (sgRNA) targeting exon 5 of MORC2 (5′-ACACCTGAGTCTACTCAGAT-3′) was designed using the online tool (http://crispor.tefor.net/). Two DNA oligos with complementary sgRNA targeting sequence and additional bases were designed as previously described[57,58]. These oligos were annealed and cloned into pLentiCRISPR v2 (Addgene plasmid #52961) to generate the MORC2 knockout vector. After transfection and puromycin selection, MORC2-deleted cells were obtained. Individual cells were sorted into separate wells of a culture plate to establish monoclonal cell lines using flow cytometry. To validate the knockout cell lines, genomic DNA was extracted from both WT and KO cells. The specific regions targeted by the sgRNA were amplified using PCR with primers: 5′-CAACATTCTCGAGCTGGACCTACAG-3′ (forward) and 5′-CCACGACAAGACTGGAAACGTGACTC-3′ (reverse). The PCR products were purified and subjected to Sanger sequencing, revealing the deletion and insertion mutations in the target sites of the MORC2 allelic genes (Fig. S2d).

Generation of endogenous EGFP-MORC2 chimeric mice

CRISPR-Cas9 was used to generate EGFP-MORC2 chimeric mice. The EGFP and linker sequence were inserted at the N-terminus of the mouse *MORC2a* gene. Briefly, a single-guide RNA (sgRNA) was designed to target exon 1 of *MORC2a*, with the sequence GACTGAAGACTCATTGCTGTCA. A donor DNA fragments containing the EGFP-linker region flanked by homologous arms was constructed. Fertilized mouse zygotes were collected, and a mixture of Cas9 mRNA (50 ng/μL), sgRNA (25 ng/μL), and donor DNA (50 ng/μL) was microinjected into pronucleus of the zygotes. The injected embryos were transferred into the oviducts of pseudopregnant recipient female mice. Resulting pups were genotyped by PCR and Sanger sequencing to confirm transgene integration (Fig. S2f). The genotyping primers for the EGFP-MORC2 allele were as follows: Left-F1: GCGGTGGTTGAGTTCCAATTCC; Left-R1: CTTCAGGGTCAGCTTGCCGTAG; Right-F1: GAACGGCATCAAGGTGAACTTC; Right-R1: TGTATCCAAGGTAATCTCTGTGGTA.

Mice were bred at the Animal Center of the University of Science and Technology of China (USTC). Animals were housed under controlled conditions (22 °C, 12-hour light/dark cycle) with free access to food and water ad libitum. All experimental procedures were approved by the Institutional Animal Care and Use Committee (IACUC) of the University of Science and Technology of China (Hefei, China).

Fluorescence recovery after photobleaching (FRAP)

The FRAP assay was performed to investigate the dynamics of protein mobility within condensates, either in *in vivo* or *in vitro*. Specific regions of interest (ROIs) approximately 2 μm² in size were selected and subjected to photobleaching using 100% laser power (488 nm) for approximately 20 ns. One droplet was left unbleached as a control. Fluorescence recovery within the ROI was monitored for 100-300 seconds. FRAP was performed using a 63x oil immersion objective mounted on a Nikon confocal microscope (in cells) or a Zeiss LSM 880 (in vitro). Fluorescence intensity was normalized to the pre-bleach signal to analyze the recovery kinetics. For brain

slice FRAP, organotypic brain slices were prepared from adult chimeric mice expressing endogenous EGFP-MORC2, following a slightly modified protocol previously described[59]. After decapitation, brains were rapidly extracted and placed in ice-cold dissection medium consisting of Hibernate A, 2% B27 supplement, 2 mM L-glutamine, and 1% penicillin–streptomycin. The cerebellum and midbrain were removed, and the remaining cerebral hemispheres were coronally sectioned at 250 μm using a McIlwain tissue chopper. Slices were gently separated in chilled dissection medium and transferred onto glass-bottom dishes containing culture medium composed of Neurobasal A, 2% B27 supplement, 2 mM L-glutamine, and 1% penicillin–streptomycin. Imaging was initiated immediately after brain slice preparation. FRAP experiments were performed using the Nikon confocal microscope. Photobleaching was carried out with 5-7 laser pulses (50 μs dwell time), and images were acquired at 2-s intervals. Post-bleach images were acquired 20 s after photobleaching.

Electrophoretic mobility shift assays (EMSA)

Widom 601 DNA (147 bp, 25 nM) was amplified by PCR and incubated with increasing concentrations of MORC2 or its domain constructs in binding buffer (20 mM Tris-HCl, pH 7.5, 45 mM KCl, 4 mM $MgCl_2$, 5% glycerol, 5 mM DTT). The reaction mixture was loaded onto a 6% polyacrylamide gel and electrophoresed at 120 V for 70 minutes. DNA was visualized using SYBR Gold stain, and images were captured using the ChemiDoc MP Imaging System.

Size-exclusion chromatography coupled with static light scattering

The analysis was performed using an AKTA FPLC system (GE Healthcare) coupled to a static light scattering detector (miniDawn, Wyatt) and a differential refractive index detector (Optilab, Wyatt). Protein samples (70 μM) were filtered and applied to a Superdex 200 increase or Superose 6 increase column, pre-equilibrated with a column buffer containing 50 mM Tris-HCl, pH 8.0, 150 mM NaCl or 1000 mM

NaCl (MORC2FL), 1 mM EDTA, and 1 mM DTT. Data were analyzed using ASTRA6 software (Wyatt).

In vitro phase separation and fluorescence microscopy imaging

Droplet formation was monitored using differential interference contrast (DIC) and fluorescence microscopy. To induce phase separation, protein was added to phase separation buffer (50 mM Tris-HCl, pH 8.0, 150 mM NaCl, 1 mM DTT). For consistency, all MORC2 samples were diluted to a final concentration of 4 μM with phase separation buffer containing 200 mM NaCl, unless otherwise specified. All preparation steps were performed at 4 °C to preserve protein activity. The phase separation mixtures were then equilibrated at room temperature for 20 min. A 5-10 μL aliquot of each sample was placed onto a custom-made glass slide, covered with an 18 mm diameter coverslip, and incubated at room temperature for 20 min before imaging.

Protein isotope labeling and NMR Spectroscopy

Isotopically labeled protein samples were expressed in minimal M9/H_2O or M9/D_2O medium. Uniformly ^{15}N-labeled (or ^{13}C- or ^{15}N-labeled) protein samples were prepared in M9/H_2O medium supplemented with 1 g/L of $^{15}NH_4Cl$ and 2 g/L of glucose (or ^{13}C-glucose). The cells were harvested at an OD_{600} of approximately 1.0. Isotope-labeled precursors and amino acids were purchased from Cambridge Isotope Laboratories (CIL). Isotopically labeled samples were prepared in 50 mM Tris-HCl, pH 8.0, 100 mM NaCl, and 7% D_2O. NMR experiments were performed using Bruker Avance III 600 MHz spectrometers equipped with a cryo-probe. NMR spectra of MORC2 and its complex were recorded at 283 K (for CC3-IBD/CC3/IBD). Protein concentrations ranged from 0.5 to 1.0 mM, and nucleotides were added to a final concentration of 10 mM. All NMR spectra were processed using NMRPipe and analyzed with NMRViewJ software (http://www.onemoonscientific.com).

Fluorescence polarization Assay (FP)

Fluorescence polarization (FP) assays were performed at room temperature (25 °C) using a BioTek H1 fluorescence spectrophotometer to evaluate the binding affinity between MORC2 protein and 5-carboxyfluorescein (5-FAM)-labeled 601 DNA (FAM-601) across a concentration range of 0-2000 nM. The 147-bp Widom 601 DNA fragment was generated via PCR amplification using a 5-FAM-labeled primer. The labeled primer was dissolved in 0.1 M $NaHCO_3$ buffer, pH 8.3, and the amplified product was purified by agarose gel extraction to eliminate residual primers and nonspecific amplification products.

Fluorescence measurements were carried out in assay buffer (50 mM Tris-HCl, pH 8.0, 150 mM NaCl, 1 mM EDTA, 1 mM DTT, and 10% glycerol) containing purified FAM-601 DNA at a final concentration of 0.4 ng/μL. Excitation and emission wavelengths were optimized according to the instrument manual, with excitation set at 485 nm and emission at 525 nm. Fluorescence polarization values were recorded in triplicate, and control measurements were included to correct for background signals.

Data were analyzed to determine the equilibrium dissociation constant (K_d) for the MORC2-FAM-601 interaction by fitting data to a log(agonist) vs. response model. In parallel, the effect of small molecules on this binding interaction was assessed by introducing compounds into the assay mixture and monitoring changes in fluorescence polarization.

ATPase activity measurements

ATPase activity was measured using 1 μM MORC2 or its mutant variant at 37 °C in 50 mM Tris-HCl, pH 8.0, 150 mM NaCl, 8 mM $MgCl_2$, 10% glycerol and 5 mM ATP[60]. All experiments were repeated independently at least three times.

RNA-seq and bioinformatic analysis

MORC2-knockout HeLa cells were seeded at equal density and transfected with 3 μg of plasmid DNA and 12 μg of PEI (polyethylenimine) per dish. After 6 hours, the transfection medium was replaced with fresh complete medium, and cells were incubated for an additional 48 hours. Cells were then washed twice with ice-cold PBS

and lysed directly in RNA Isolator (R401, Vazyme) on ice. Total RNA was extracted using the RNeasy Mini Kit (Qiagen, 74004) according to the manufacturer's protocol. RNA quality was assessed using NanoDrop 2000 (Thermo Fisher Scientific), Agilent 2100 Bioanalyzer, and LabChip GX (PerkinElmer). For library preparation, 1 μg of total RNA was used per sample, employing the VAHTS Universal V6 RNA-seq Library Prep Kit for MGI®. The resulting double-stranded DNA libraries were denatured, circularized, and digested to obtain single-stranded circular DNA. DNA nanoballs (DNBs) were generated from these templates through rolling circle amplification (RCA). Sequencing was performed on the MGI DNBSEQ-T7 platform (MGI Tech Co., Ltd) using combinatorial Probe-Anchor Synthesis (cPAS) chemistry.

Before performing differential expression analysis, lowly expressed genes were filtered out by retaining only those with a raw count of ≥10 in at least three samples. Differential gene expression analysis between sample groups was carried out using the DESeq2 package (v1.26.0). Genes with an absolute fold change > 1.2 or < 0.83, and $p < 0.05$ were defined as differentially expressed genes (DEGs). These DEGs were subsequently subjected to Gene Ontology (GO) enrichment analysis in DAVID (Knowledgebase v2025_1).

Statistical Analysis

All statistical analyses were performed in GraphPad Prism. All data underwent normality testing (D'Agostino & Pearson test and Anderson-Darling test) in advance. Two-tailed unpaired Student's *t*-test post-hoc Welch's correction and one-way ANOVA with Tukey's post hoc test was used when data were distributed normally. The significance level was set as $p < 0.05$. All statistical results are provided as Source Data.

Acknowledgments

We thank Dr. Xuebiao Yao (University of Science and Technology of China, USTC), Dr. Zhi Qi and Dr. Linyu Zuo (Peking University) for helpful discussion. We thank members of the Shanghai Synchrotron Radiation Facility (SSRF, China; beamlines BL02U1, BL18U1, and BL19U1) for X-ray beam time. This work was supported by grants from the National Key R&D Program of China (2020YFA0710700, 2023YFC3403102, 2019YFA0508402, and 2022YFC2303300), the National Natural Science Foundation of China (52025036, 22122703, 32470808, 32170767, 31770807, 31971144, 82201533, 82203848 and T2221005), the Center for Advanced Interdisciplinary Science and Biomedicine of IHM (QYPY20220014), the Strategic Priority Research Program of the Chinese Academy of Sciences (XDB0490000), the Major Frontier Research Project of USTC (LS9100000002), USTC Research Funds of Double First-Class Initiative (YD9100002507 and YD9100002054), the Anhui Medical University Foundation (9101224201), and National Natural Science Foundation Incubation Program of The Second Affiliated Hospital of Anhui Medical University (2021GQFY02).

Author contributions

Y.B., Y.Z., W.D., W.X., C.H., Y.W., and C.W. designed the experiments. Y.B., Y.Z., W.D., and W.X. conducted the experiments. Y.Z. determined the crystal structure. Y.W., W.J. and F.Z. assisted with the experiments and reagents. All authors analyzed the data. Y.B., Y.Z., C.H., Y.W., and C.W. wrote the manuscript with input from all authors. All authors approved the final version of the manuscript.

Competing interests

The authors declare that they have no competing interests.

Data and materials availability

All data needed to evaluate the conclusions in the paper are present in the paper

and/or the Supplementary Materials. Raw gene expression data are available in Source Data. The atomic coordinates of the MORC2 CC3 domain have been deposited to the Protein Data Bank under the accession code: 9KQL.

References

1. Alabert, C. & Groth, A. Chromatin replication and epigenome maintenance. *Nat Rev Mol Cell Biol* **13**, 153–167 (2012).
2. Ishihara, S. *et al.* Local states of chromatin compaction at transcription start sites control transcription levels. *Nucleic Acids Res* **49**, 8007–8023 (2021).
3. Downs, J. A. & Gasser, S. M. Chromatin remodeling and spatial concerns in DNA double-strand break repair. *Curr Opin Cell Biol* **90**, 102405 (2024).
4. Blackledge, N. P. & Klose, R. J. The molecular principles of gene regulation by Polycomb repressive complexes. *Nat Rev Mol Cell Biol* **22**, 815–833 (2021).
5. Li, D.-Q. *et al.* MORC2 signaling integrates phosphorylation-dependent, ATPase-coupled chromatin remodeling during the DNA damage response. *Cell Rep* **2**, 1657–1669 (2012).
6. Müller, I. & Helin, K. Keep quiet: the HUSH complex in transcriptional silencing and disease. *Nat Struct Mol Biol* **31**, 11–22 (2024).
7. Zhong, Z. *et al.* MORC proteins regulate transcription factor binding by mediating chromatin compaction in active chromatin regions. *Genome Biol* **24**, 96 (2023).
8. Xue, Y. *et al.* Arabidopsis MORC proteins function in the efficient establishment of RNA directed DNA methylation. *Nat Commun* **12**, 4292 (2021).
9. Weiser, N. E. *et al.* MORC-1 Integrates Nuclear RNAi and Transgenerational Chromatin Architecture to Promote Germline Immortality. *Developmental Cell* **41**, 408-423.e7 (2017).
10. Moissiard, G. *et al.* MORC family ATPases required for heterochromatin condensation and gene silencing. *Science* **336**, 1448–1451 (2012).
11. Wang, H., Zhang, L., Luo, Q., Liu, J. & Wang, G. MORC protein family-related signature within human disease and cancer. *Cell Death Dis* **12**, 1112 (2021).
12. Tchasovnikarova, I. A. *et al.* Hyperactivation of HUSH complex function by Charcot-Marie-Tooth disease mutation in MORC2. *Nature Genetics* (2017) doi:10.1038/ng.3878.
13. Douse, C. H. *et al.* Neuropathic MORC2 mutations perturb GHKL ATPase dimerization dynamics and epigenetic silencing by multiple structural mechanisms. *Nat Commun* **9**, 651 (2018).
14. Xie, H.-Y., Zhang, T.-M., Hu, S.-Y., Shao, Z.-M. & Li, D.-Q. Dimerization of MORC2 through its C-terminal coiled-coil domain enhances chromatin dynamics and promotes DNA repair. *Cell Commun Signal* **17**, 160 (2019).
15. Morais Cabral, J. H. *et al.* Crystal structure of the breakage-reunion domain of DNA gyrase. *Nature* **388**, 903–906 (1997).
16. Chen, K. *et al.* Crystal structure of the hinge domain of Smchd1 reveals its dimerization mode and nucleic acid-binding residues. *Sci Signal* **13**, eaaz5599 (2020).
17. Liu, J. *et al.* Cascading MutS and MutL sliding clamps control DNA diffusion to activate mismatch repair. *Nature* **539**, 583–587 (2016).
18. Ortega, J., Lee, G. S., Gu, L., Yang, W. & Li, G.-M. Mispair-bound human MutS-MutL complex triggers DNA incisions and activates mismatch repair. *Cell Res* **31**, 542–553 (2021).
19. Lee, K. *et al.* The structure of an Hsp90-immunophilin complex reveals cochaperone recognition of the client maturation state. *Mol Cell* **81**, 3496-3508.e5 (2021).
20. Pastor, W. A. *et al.* MORC1 represses transposable elements in the mouse male germline. *Nat*

Commun **5**, 5795 (2014).
21. Dopkins, N. *et al.* A field guide to endogenous retrovirus regulatory networks. *Mol Cell* **82**, 3763–3768 (2022).
22. Fendler, N. L. *et al.* Identification and characterization of a human MORC2 DNA binding region that is required for gene silencing. *Nucleic Acids Res* **53**, gkae1273 (2025).
23. Leidescher, S. *et al.* Spatial organization of transcribed eukaryotic genes. *Nat Cell Biol* **24**, 327–339 (2022).
24. Membrane-less compartments in the nucleus: Separated or connected phases? *Current Opinion in Cell Biology* **84**, 102215 (2023).
25. Boeynaems, S. *et al.* Protein Phase Separation: A New Phase in Cell Biology. *Trends Cell Biol* **28**, 420–435 (2018).
26. Yoshizawa, T. *et al.* Nuclear Import Receptor Inhibits Phase Separation of FUS through Binding to Multiple Sites. *Cell* **173**, 693-705.e22 (2018).
27. Verba, K. A. *et al.* Atomic structure of Hsp90-Cdc37-Cdk4 reveals that Hsp90 traps and stabilizes an unfolded kinase. *Science* **352**, 1542–1547 (2016).
28. Alberti, S., Gladfelter, A. & Mittag, T. Considerations and Challenges in Studying Liquid-Liquid Phase Separation and Biomolecular Condensates. *Cell* **176**, 419–434 (2019).
29. Zhang, Y. *et al.* MORC3 Forms Nuclear Condensates through Phase Separation. *iScience* **17**, 182–189 (2019).
30. Kalderon, D., Roberts, B. L., Richardson, W. D. & Smith, A. E. A short amino acid sequence able to specify nuclear location. *Cell* **39**, 499–509 (1984).
31. Alderson, T. R. & Kay, L. E. NMR spectroscopy captures the essential role of dynamics in regulating biomolecular function. *Cell* **184**, 577–595 (2021).
32. Kim, T. H. *et al.* Phospho-dependent phase separation of FMRP and CAPRIN1 recapitulates regulation of translation and deadenylation. *Science* **365**, 825–829 (2019).
33. Murthy, A. C. *et al.* Molecular interactions underlying liquid−liquid phase separation of the FUS low-complexity domain. *Nat Struct Mol Biol* **26**, 637–648 (2019).
34. Pandiloski, N. *et al.* DNA methylation governs the sensitivity of repeats to restriction by the HUSH-MORC2 corepressor. *Nat Commun* **15**, 7534 (2024).
35. Fukuda, K., Okuda, A., Yusa, K. & Shinkai, Y. A CRISPR knockout screen identifies SETDB1-target retroelement silencing factors in embryonic stem cells. *Genome Res* **28**, 846–858 (2018).
36. Liu, N. *et al.* Selective silencing of euchromatic L1s revealed by genome-wide screens for L1 regulators. *Nature* **553**, 228–232 (2018).
37. Jacquier, A., Roubille, S., Lomonte, P. & Schaeffer, L. Microrchidia CW-Type Zinc Finger 2, a Chromatin Modifier in a Spectrum of Peripheral Neuropathies. *Front Cell Neurosci* **16**, 896854 (2022).
38. Stafki, S. A. *et al.* The Spectrum of MORC2-Related Disorders: A Potential Link to Cockayne Syndrome. *Pediatr Neurol* **141**, 79–86 (2023).
39. Chung, H. Y. *et al.* Morc2a variants cause hydroxyl radical-mediated neuropathy and are rescued by restoring GHKL ATPase. *Brain* **147**, 2114–2127 (2024).
40. Ding, Q.-S. *et al.* Aberrant high expression level of MORC2 is a common character in multiple cancers. *Hum Pathol* **76**, 58–67 (2018).
41. Zhang, S. *et al.* Oncogenic MORC2 in cancer development and beyond. *Genes Dis* **11**, 861–

873 (2024).
42. Li, D.-Q., Nair, S. S. & Kumar, R. The MORC family: new epigenetic regulators of transcription and DNA damage response. *Epigenetics* **8**, 685–693 (2013).
43. Koch, A. *et al.* MORC Proteins: Novel Players in Plant and Animal Health. *Front Plant Sci* **8**, 1720 (2017).
44. Dong, W. *et al.* MORC Domain Definition and Evolutionary Analysis of the MORC Gene Family in Green Plants. *Genome Biol Evol* **10**, 1730–1744 (2018).
45. Inoue, N. *et al.* New gene family defined by MORC, a nuclear protein required for mouse spermatogenesis. *Hum Mol Genet* **8**, 1201–1207 (1999).
46. Wang, G.-L. *et al.* Identification and expression analysis of a novel CW-type zinc finger protein MORC2 in cancer cells. *Anat Rec (Hoboken)* **293**, 1002–1009 (2010).
47. Guddeti, R. K., Chutani, N. & Pakala, S. B. MORC2 Interactome: Its Involvement in Metabolism and Cancer. *Biophys Rev* **13**, 507–514 (2021).
48. Tencer, A. H. *et al.* Molecular mechanism of the MORC4 ATPase activation. *Nat Commun* **11**, 5466 (2020).
49. Prasanth, M. I. *et al.* Role of Epigenetic Modulation in Neurodegenerative Diseases: Implications of Phytochemical Interventions. *Antioxidants (Basel)* **13**, 606 (2024).
50. Zhang, L., Zhang, L. & Li, D.-Q. MORC2 regulates DNA damage response through a PARP1-dependent pathway. *Nucleic Acids Research* (2019) doi:10.1093/nar/gkz545.
51. Tunbak, H. *et al.* The HUSH complex is a gatekeeper of type I interferon through epigenetic regulation of LINE-1s. *Nat Commun* **11**, 5387 (2020).
52. Pandiloski, N. *et al.* DNA methylation governs the sensitivity of repeats to restriction by the HUSH-MORC2 corepressor. *Nat Commun* **15**, 7534 (2024).
53. Vuzman, D. & Levy, Y. Intrinsically disordered regions as affinity tuners in protein-DNA interactions. *Mol Biosyst* **8**, 47–57 (2012).
54. van der Lee, R. *et al.* Classification of intrinsically disordered regions and proteins. *Chem Rev* **114**, 6589–6631 (2014).
55. Ukmar-Godec, T. *et al.* Lysine/RNA-interactions drive and regulate biomolecular condensation. *Nat Commun* **10**, 2909 (2019).
56. Ukmar-Godec, T. *et al.* Multimodal interactions drive chromatin phase separation and compaction. *Proceedings of the National Academy of Sciences* **120**, e2308858120 (2023).
57. Shalem, O. *et al.* Genome-scale CRISPR-Cas9 knockout screening in human cells. *Science* **343**, 84–87 (2014).
58. Sanjana, N. E., Shalem, O. & Zhang, F. Improved vectors and genome-wide libraries for CRISPR screening. *Nat Methods* **11**, 783–784 (2014).
59. Li, C. H. *et al.* MeCP2 links heterochromatin condensates and neurodevelopmental disease. *Nature* **586**, 440–444 (2020).
60. Microtiter assay for glutamine synthetase biosynthetic activity using inorganic phosphate detection. *Analytical Biochemistry* **327**, 114–118 (2004).

Figure legends

Fig. 1 The CC3 domain serves as the structural basis for full-length MORC2 dimerization.

(a) The domain organization of human MORC2FL, highlighting the ATPase module (GHL, CC1 and S5 domains, collectively termed NTD), the C-terminal domains (CTD) with coiled-coil regions (CC2 and CC3), CW-type zinc finger (CW), intrinsically disordered region (IDR, marked by a fresh green line by IUPRED2 prediction), nuclear localization signal (NLS), Tudor-chromodomain (TCD), and a 30-residues tail domain (IBD).

(b) Purification and characterization of full-length human MORC2 in HEK293F cell system. SDS-PAGE analysis of the purified protein demonstrates its purity and distribution.

(c) Static light-scattering (SLS) analysis shows that MORC2 forms dimers in the absence of ATP, with a molecular weight of 239 ± 1 kDa in standard buffer (mint green line) and 303 ± 2 kDa in the presence of 601 DNA (sunflower yellow line).

(d) SLS analysis reveals the oligomerization states of MORC2 truncations. Full-length MORC2 lacking CC3-IBD (1-900) is monomeric, while CC3-IBD (901-1032) and CC3 alone (901-1003) form stable dimers.

(e) Crystal structural of the CC3 dimer. Hydrophobic residues contributing to dimer stability (L911, L915, and F922) are highlighted using ball-and-stick representations. Top view of the hydrophobic core of the CC3 dimer. Layers of hydrophobic contacts stabilize the dimer interface, illustrated with paired residues (e.g., Layer 1: L911-L911’, Layer 2: L915-L915’, and Layer 3: F922-F922’).

(f) Additional SLS analysis confirms that fragments spanning residues 537-1032, 744-1032, and Trx-901-975 (CC3 truncation) adopt dimeric conformations.

Fig. 2 MORC2 undergoes liquid-liquid phase separation (LLPS) under physiological conditions.

(a) SDS-PAGE analysis of EGFP-MORC2FL protein purified from HEK293F cells, showing protein concentration at 2.5 μM and 5 μM.

(b) Sedimentation assay shows the distribution of EGFP-MORC2FL (7.2 μM) between supernatant (S) and pellet (P) fractions under 1000 mM (control) and 150 mM NaCl, indicating its propensity for phase separation.

(c) EGFP-MORC2 (7.2 μM) undergoes phase separation into droplets in a buffer containing 150 mM NaCl, but not in 1000 mM NaCl buffer. Scaler bar: 2 μm.

(d) The proteins were examined in a buffer containing 150 mM NaCl, and phase separation was assessed by fluorescence microscopy with 488 nm excitation for EGFP. Quantification of droplet areas from (Fig. S2a), presented as violin plots with box plots indicating medians. Data are derived from ≥ 3 independent images and reflect the size distribution of phase-separated droplets. Data are presented as mean ± SEM; one-way ANOVA with Tukey's post hoc test. ****$p < 0.0001$; *$p < 0.05$.

(e) Time-lapse FRAP imaging of EGFP-MORC2FL droplets formed *in vitro*, demonstrating fluorescence recovery over time. Scaler bar: 2 μm.

(f) Quantitative analysis of fluorescence recovery from (e), showing the dynamic properties of *in vitro* MORC2 droplets. Data represent mean ± SEM, with $n \geq 3$ replicates.

(g) Immunostaining of endogenous MORC2 in HeLa cells revealed punctate localized within the nucleus, likely representing condensates involved in transcriptional regulation (white arrows). Nuclei are counterstained with DAPI to visualize chromatin-rich regions. Scaler bar: 5 μm.

(h) Live-cell imaging of transiently transfected EGFP-MORC2FL showed its assembly into dispersed, nearly spherical condensates in the nucleus, while stable expression of H2A-mCherry served to mark chromatin-enriched domains. Scaler bar: 10 μm.

(i) Time-lapse FRAP analysis of EGFP-MORC2FL condensates in the nuclei of

transiently transfected HeLa cells revealed rapid fluorescence recovery within seconds, indicative of their dynamic, liquid-like nature. Scaler bar: 1 μm.

(j) Quantitative analysis of fluorescence recovery from (i), showing the dynamic properties of *in vitro* MORC2 droplets. Data represent mean ± SEM, with n ≥ 10 replicates.

(k) Sections of brain and spinal cord from endogenous EGFP-MORC2 chimeric mice show EGFP-MORC2 condensation distribution in NeuN-positive neurons. Scaler bar: 10 μm.

(l) Representative FRAP images from of FRAP experiments performed on fresh 250-μm brain slices of endogenous EGFP-MORC2 chimeric mice demonstrate the dynamic nature of endogenous MORC2 condensates. Data are presented as mean ± SEM, with $n = 3$ droplets analyzed. Scaler bar: 5 μm.

Fig. 3 Multiple domains regulate phase separation of MORC2.

(a) Sequential deletion analysis revealed that the NTD is dispensable for condensate formation, as EGFP-tagged NTD alone failed to form condensates and was excluded from the nucleus. Fusion with a canonical nuclear localization signal ("PKKKRKV") restored nuclear localization but did not rescue condensate formation. In contrast, the CTD alone was sufficient to form nuclear condensates. Deletion of the CW domain resulted in enlarged condensates in a subset of cells, while removal of CC2 or the TCD had no apparent effect on condensate formation. Strikingly, deletion of either the IDR or CC3 completely abolished nuclear condensate assembly. Deletion of the IBD markedly reduced the frequency of condensate formation. Loss of the intrinsic NLS led to cytoplasmic localization of MORC2; however, no condensates were detected in the cytoplasm under transient transfection conditions in HeLa cells. Together, these results define the IDR and CC3 as the minimal and essential elements for MORC2-mediated phase separation, and implicate the CW domain, IBD, and nuclear microenvironment in the fine-tuning of condensate assembly. Scaler bar: 10 μm.

(b) *In vitro* phase separation of Cy3-labeled CTDΔCW at concentrations from 1.25 μM to 20 μM in 150 mM NaCl buffer, visualized as spherical condensates. Scaler bar: 10 μm.

(c) Quantification of droplet areas from (b), displayed as violin plots with box plots indicating median values. Data are presented as mean ± SEM; one-way ANOVA with Tukey's post hoc test. ****$p < 0.0001$, *n.s.* not significant.

(d) SDS-PAGE analysis of Cy3-CTDΔCW protein distribution between supernatant (S) and pellet (P) fractions after centrifugation at increasing concentrations (5 μM to 40 μM) in 150 mM NaCl buffer. At 40 μM, increasing the NaCl concentration to 300 mM or 500 mM reduced droplet formation, indicating salt sensitivity.

(e) Quantification of Cy3-CTDΔCW showing the percentage of soluble protein from densitometric analysis of S/P fractions in panel (d), based on three independent biological replicates.

Fig. 4 Multivalent interactions between IDR and IBD drive MORC2 LLPS.

(a) Domain organization of MORC2 C-terminal regions analyzed by NMR titration, including the IDR, CC3, and IBD.

(b) ^{15}N-labeled CC3 (residues 901–1003) shows no chemical shift upon titration with IDR (residues 593–735), indicating no detectable interaction.

(c) ^{15}N-labeled IBD (residues 1004–1032) exhibits clear chemical shift perturbations (CSPs) upon IDR titration, confirming a direct, specific interaction.

(d-f) NMR titrations of ^{15}N-labeled IBD with IDR subregions: IDRa (593–643), IDRb (644–694), and IDRc (695–735). IDRa induces clear CSPs (d), while IDRb (e) and IDRc (f) show minimal or no shifts, identifying IDRa as the primary IBD-binding segment.

(g) Sequence analysis of IDR subregions reveals that IDRa is enriched in proline and arginine residues, enabling electrostatic interactions. Sequence alignment of IBD across species highlights conserved residues involved in IDRa binding. A summary table lists representative residues from IDRa and IBD exhibiting CSPs in titration assays (marked with asterisks).

(h) Representative confocal images of HeLa cells expressing EGFP-tagged MORC2ΔIDRa, ΔIDRb, or ΔIDRc constructs. Scale bar: 10 μm.

(i) Quantification of droplet area per cell in (h). Deletion of IDRa significantly impairs condensate formation. n = 10 cells per condition. Data are presented as mean ± SEM; statistical analysis: one-way ANOVA with Tukey's post hoc test. ***$p < 0.001$; *n.s.* not significant.

(j) Working model of MORC2 LLPS. CC3 dimerization serves as a structural scaffold, while weak, transient, but specific multivalent interactions between IDRa and IBD cooperatively promote condensate formation.

Fig. 5 DNA binding enhances MORC2 phase separation and modulates its ATPase activity.

(a) Electrophoretic mobility shift assay (EMSA) showing that MORC2FL binds 25 nM 601 DNA, as evidenced by shifts in DNA mobility corresponding to protein-DNA complexes.

(b) EMSA highlighting the strong DNA-binding affinity of the CC1 domain, corroborating previous reports that identify this region as a key mediator of DNA interaction.

(c-f) EMSA results demonstrating the binding capacities of individual MORC2 domains to 25 nM 601 DNA: CC2 (c), IDR (d), TCD-CC3-IBD (e), and CC3-IBD (f). The IDR exhibits robust DNA-binding activity, CC2 and TCD-CC3-IBD show weaker interactions, and CC3-IBD alone fails to bind DNA. These findings identify CC1, CC2, IDR, and the TCD as DNA-binding domains of MORC2.

(g) Confocal imaging showing that 601 DNA promotes MORC2 phase separation. At 0.9 μM, EGFP-MORC2FL alone does not form droplets, but the addition of 25 nM 601 DNA induces distinct condensate formation. Scaler bar: 5 μm.

(h) Quantification of MORC2 condensate sizes with or without 601 DNA. Violin plots illustrate the distribution of droplet sizes, with box plots indicating median values. Data are presented as mean ± SEM; unpaired student *t*-test. ****$p < 0.0001$.

(i) Fluorescence microscopy showing Cy3-labeled CTDΔCW (1.25 μM) coalescing with 25 nM FAM-labeled 601 DNA. DNA is recruited into MORC2 droplets, forming distinct condensates. Scaler bar: 5 μm.

(j) In the presence of 10 nM 601 DNA, the ATP hydrolysis activity of MORC2FL is significantly enhanced. The N39A mutant, which is deficient in ATP binding, serves as a negative control; nevertheless, a slight but detectable increase in ATPase activity is observed upon DNA binding. ATP hydrolysis activity of MORC2FL is significantly increased in the presence of 10 nM 601 DNA. The N39A mutant, which is deficient in ATP binding, serves as a negative control. Data are presented as mean ± SEM; statistical analysis: one-way ANOVA with Tukey's post hoc test. ****$p < 0.0001$.

Fig. 6 MORC2 phase separation is required for its transcriptional regulatory activity.

(a) Schematic of the rescue experiment strategy. HeLa cells with CRISPR-Cas9-mediated MORC2 knockout were reconstituted with EGFP, EGFP-MORC2FL, or phase separation-deficient mutants EGFP-MORC2ΔCC3 and EGFP-MORC2ΔIDR.

(b) RNA-seq-derived read counts for the MORC2 gene in EGFP, EGFP-MORC2FL, EGFP-MORC2ΔCC3, and EGFP-MORC2ΔIDR expressing cells.

(c-d) Venn diagram illustrating the overlap between differentially expressed genes identified following EGFP-MORC2FL overexpression in this study and previously characterized MORC2-regulated targets.

(e) Volcano plots of RNA-seq read counts for EGFP-MORC2FL and EGFP-MORC2ΔCC3 overexpression compared to EGFP control. Significantly upregulated genes are shown in yellow, and significantly downregulated genes are shown in green, based on three biological replicates (fold change > 1.2 or < 0.83, $p < 0.05$).

(f) LLPS-deficient mutant of MORC2 fails to regulate these 18 downregulated genes despite comparable protein expression levels, supporting a functional role of MORC2 condensates in transcriptional regulation.

Fig. 7 Pathogenic variants of MORC2 alter phase separation, DNA binding, and ATPase activity.

(a) Schematic illustration of pathogenic MORC2 mutations associated with Charcot-Marie-Tooth disease type 2Z (CMT2Z, red) and spinal muscular atrophy (SMA, blue), mapped onto the MORC2 domain structure.

(b) Quantification of HeLa cells transfected with WT MORC2 or nine pathogenic mutations exhibiting nuclear condensates was performed for each field of view. E236G and T424R shows the most pronounced enhancement of phase separation. n ≥ 10 fields. Data are presented as mean ± SEM; one-way ANOVA with Tukey's post hoc test. ****$p < 0.0001$, **$p < 0.01$, *n.s.* not significant.

(c) ATPase activity of WT MORC2 and eight pathogenic variants, measured under revised conditions. S218L, F256L, and T424R exhibit significantly elevated activity. We were unable to purify MORC2 constructs bearing the E236G mutation from either HEK293F cells, suggesting that it may cause misfolding of the ATPase module. Data are presented as mean ± SEM; one-way ANOVA with Tukey's post hoc test. ****$p < 0.0001$, **$p < 0.01$, *n.s.* not significant.

(d) Fluorescence polarization (FP) analysis of DNA binding affinities to the 601 DNA sequence. All protein variants were evaluated under uniform assay conditions, including those pertinent to phase separation. Dissociation constants (K_d) were determined by fitting the FP data to a log(agonist) vs. response model and are reported as mean ±SEM: WT (98 ± 1 nM), R252W (51 ± 2 nM), Q400R (145 ± 26 nM), D466N (49 ± 6 nM), S87L (107 ± 24 nM), S218L (92 ± 10 nM), F256L (69 ± 2 nM), R266A (63 ± 5 nM), and T424R (242 ± 13 nM). Several variants, including R252W, D466N, F256L, and R266A, demonstrated increased binding affinity relative to WT, while others, such as T424R and Q400R, exhibited markedly reduced binding.

(e) Proposed model summarizing the impact of DNA binding and phase separation on MORC2-mediated chromatin remodeling. DNA promotes MORC2 condensate formation through electrostatic interactions, which enhances its ability to compact chromatin and regulate transcriptional silencing.

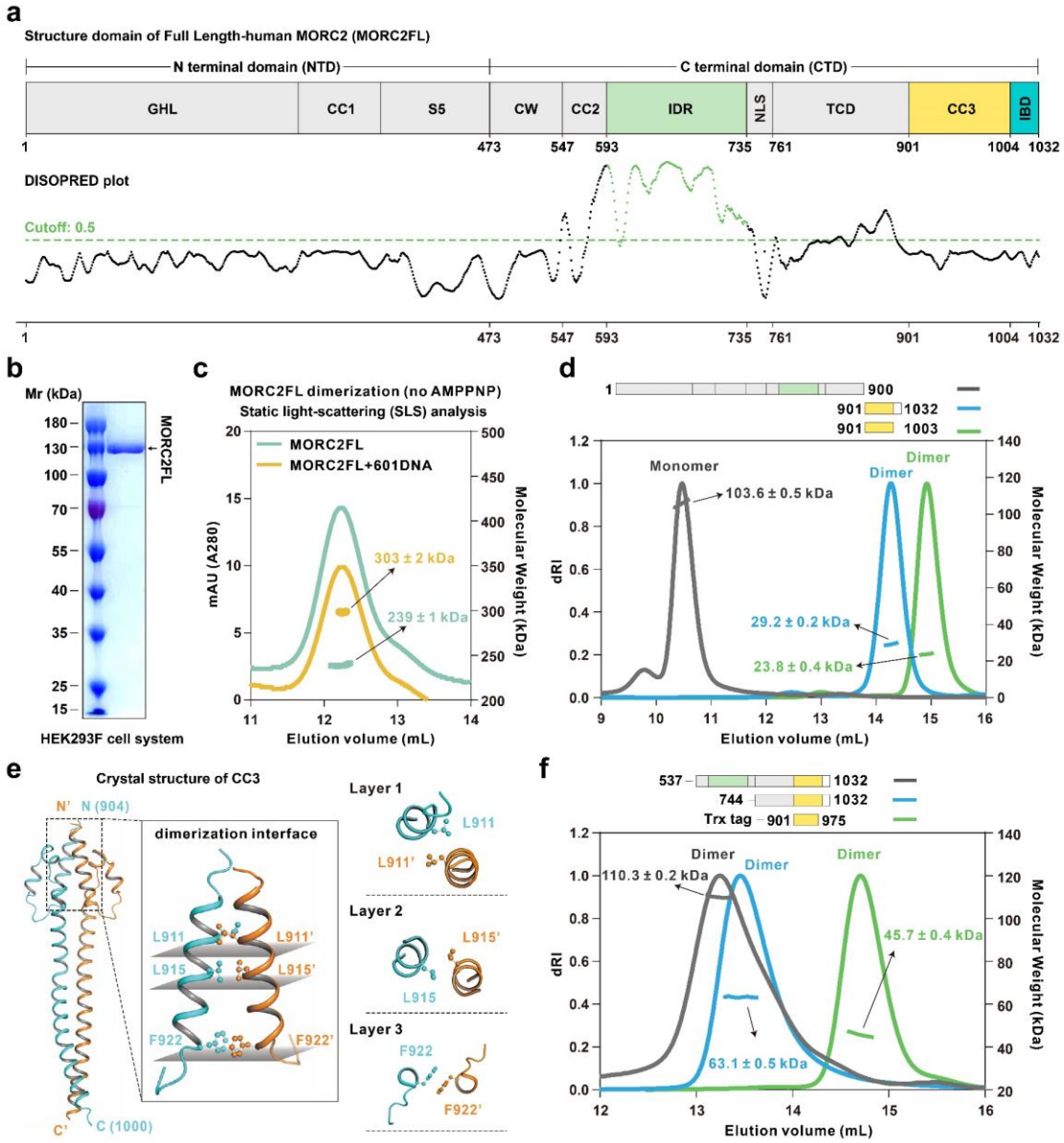
a
Structure domain of Full Length-human MORC2 (MORC2FL)
N terminal domain (NTD)
C terminal domain (CTD)
GHL
CC1
S5
CW
CC2
IDR
NLS
TCD
CC3
IBD
1
473
547
593
735
761
901
1004
1032
DISOPRED plot
Cutoff: 0.5
b
Mr (kDa)
MORC2FL
HEK293F cell system
c
MORC2FL dimerization (no AMPPNP)
Static light-scattering (SLS) analysis
MORC2FL
MORC2FL+601DNA
303 ± 2 kDa
239 ± 1 kDa
mAU (A280)
Molecular Weight (kDa)
Elution volume (mL)
d
Monomer
Dimer
103.6 ± 0.5 kDa
29.2 ± 0.2 kDa
23.8 ± 0.4 kDa
dRI
Molecular Weight (kDa)
Elution volume (mL)
e
Crystal structure of CC3
N' N (904)
dimerization interface
L911
L911'
L915
L915'
F922
F922'
C'
C (1000)
Layer 1
Layer 2
Layer 3
f
537
744
Trx tag
901
975
1032
Dimer
110.3 ± 0.2 kDa
63.1 ± 0.5 kDa
45.7 ± 0.4 kDa
dRI
Molecular Weight (kDa)
Elution volume (mL)

Figure 1

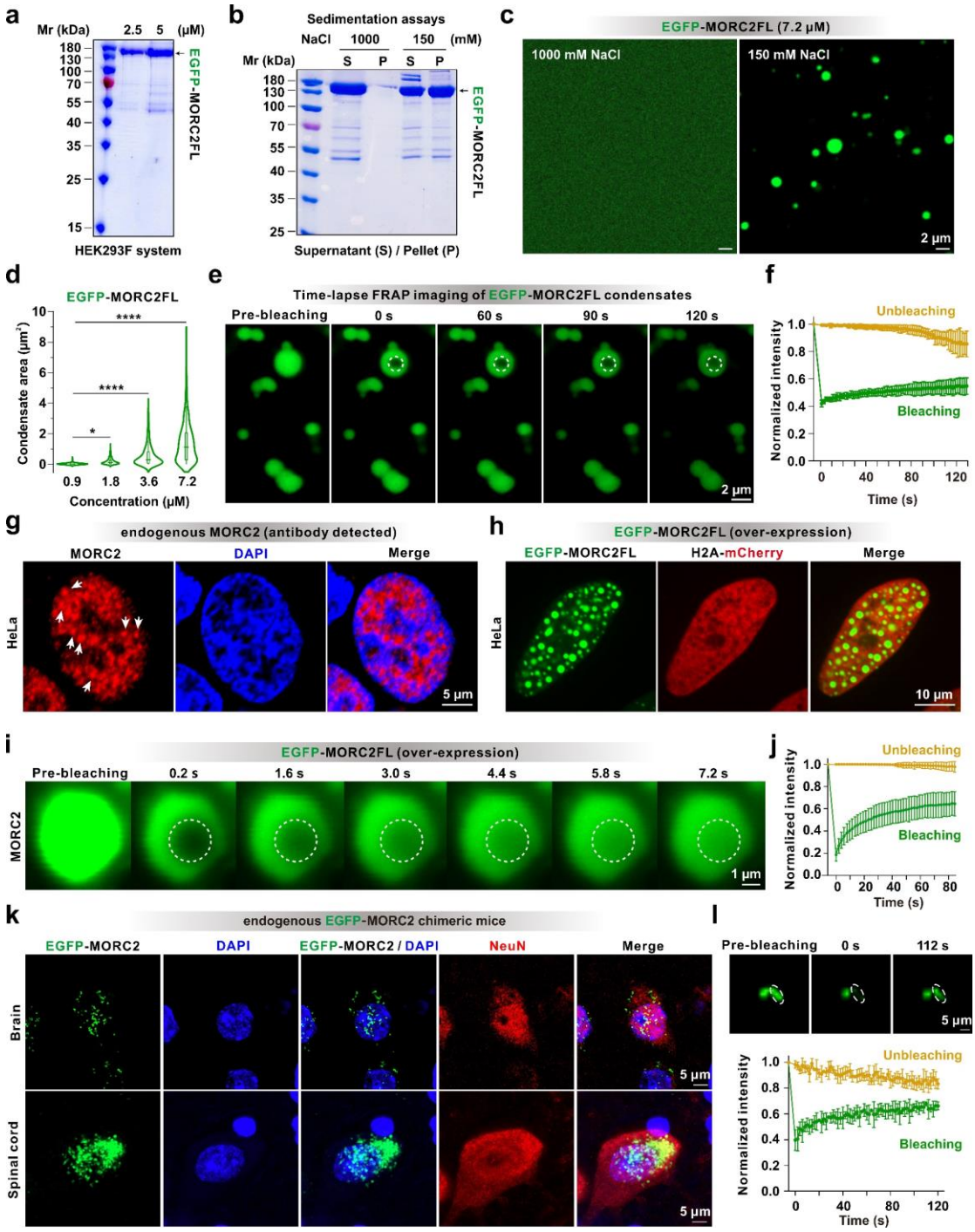
a
Mr (kDa)
2.5
5
(μM)
180
130
100
70
55
40
35
25
15
EGFP-MORC2FL
HEK293F system
b
Sedimentation assays
NaCl
1000
150
(mM)
Mr (kDa)
S
P
S
P
EGFP-MORC2FL
Supernatant (S) / Pellet (P)
c
EGFP-MORC2FL (7.2 μM)
1000 mM NaCl
150 mM NaCl
2 μm
d
EGFP-MORC2FL
Condensate area (μm²)
****
****
*
0.9
1.8
3.6
7.2
Concentration (μM)
e
Time-lapse FRAP imaging of EGFP-MORC2FL condensates
Pre-bleaching
0 s
60 s
90 s
120 s
2 μm
f
Unbleaching
Bleaching
Normalized intensity
Time (s)
g
endogenous MORC2 (antibody detected)
MORC2
DAPI
Merge
HeLa
5 μm
h
EGFP-MORC2FL (over-expression)
EGFP-MORC2FL
H2A-mCherry
Merge
HeLa
10 μm
i
EGFP-MORC2FL (over-expression)
Pre-bleaching
0.2 s
1.6 s
3.0 s
4.4 s
5.8 s
7.2 s
MORC2
1 μm
j
Unbleaching
Bleaching
Normalized intensity
Time (s)
k
endogenous EGFP-MORC2 chimeric mice
EGFP-MORC2
DAPI
EGFP-MORC2 / DAPI
NeuN
Merge
Brain
Spinal cord
5 μm
5 μm
l
Pre-bleaching
0 s
112 s
5 μm
Unbleaching
Bleaching
Normalized intensity
Time (s)

Figure 2

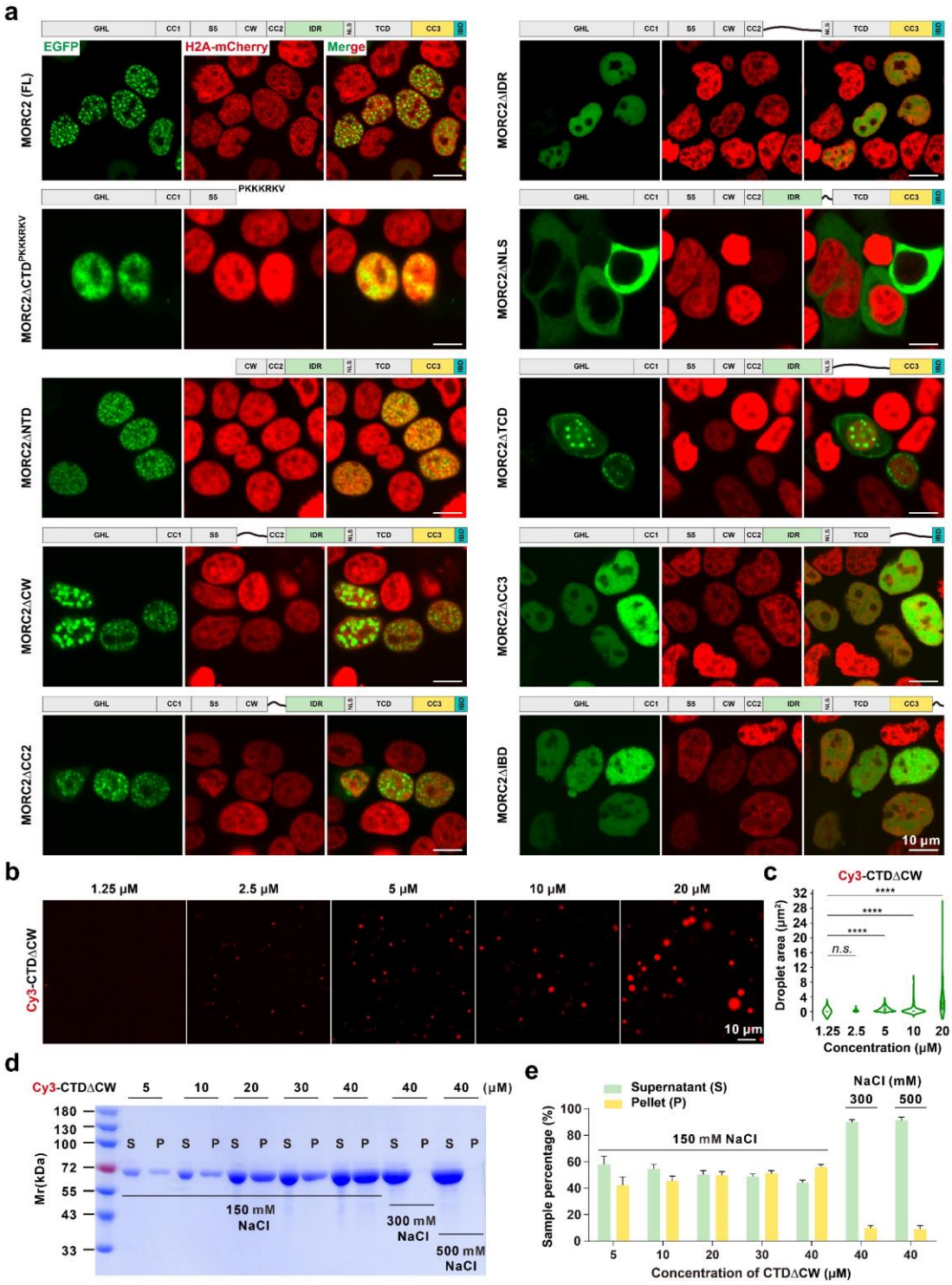
a
EGFP
H2A-mCherry
Merge
MORC2 (FL)
MORC2ΔCTD^PKKKRKV
MORC2ΔNTD
MORC2ΔCW
MORC2ΔCC2
MORC2ΔIDR
MORC2ΔNLS
MORC2ΔTCD
MORC2ΔCC3
MORC2ΔIBD
PKKKRKV
GHL
CC1
S5
CW
CC2
IDR
NLS
TCD
CC3
IBD
10 μm
b
1.25 μM
2.5 μM
5 μM
10 μM
20 μM
Cy3-CTDΔCW
10 μm
c
Cy3-CTDΔCW
Droplet area (μm²)
n.s.
****
Concentration (μM)
d
Cy3-CTDΔCW
5
10
20
30
40
40
40
(μM)
Mr(kDa)
180
130
100
72
55
43
33
S
P
150 mM NaCl
300 mM NaCl
500 mM NaCl
e
Supernatant (S)
Pellet (P)
NaCl (mM)
300
500
150 mM NaCl
Sample percentage (%)
Concentration of CTDΔCW (μM)

Figure 3

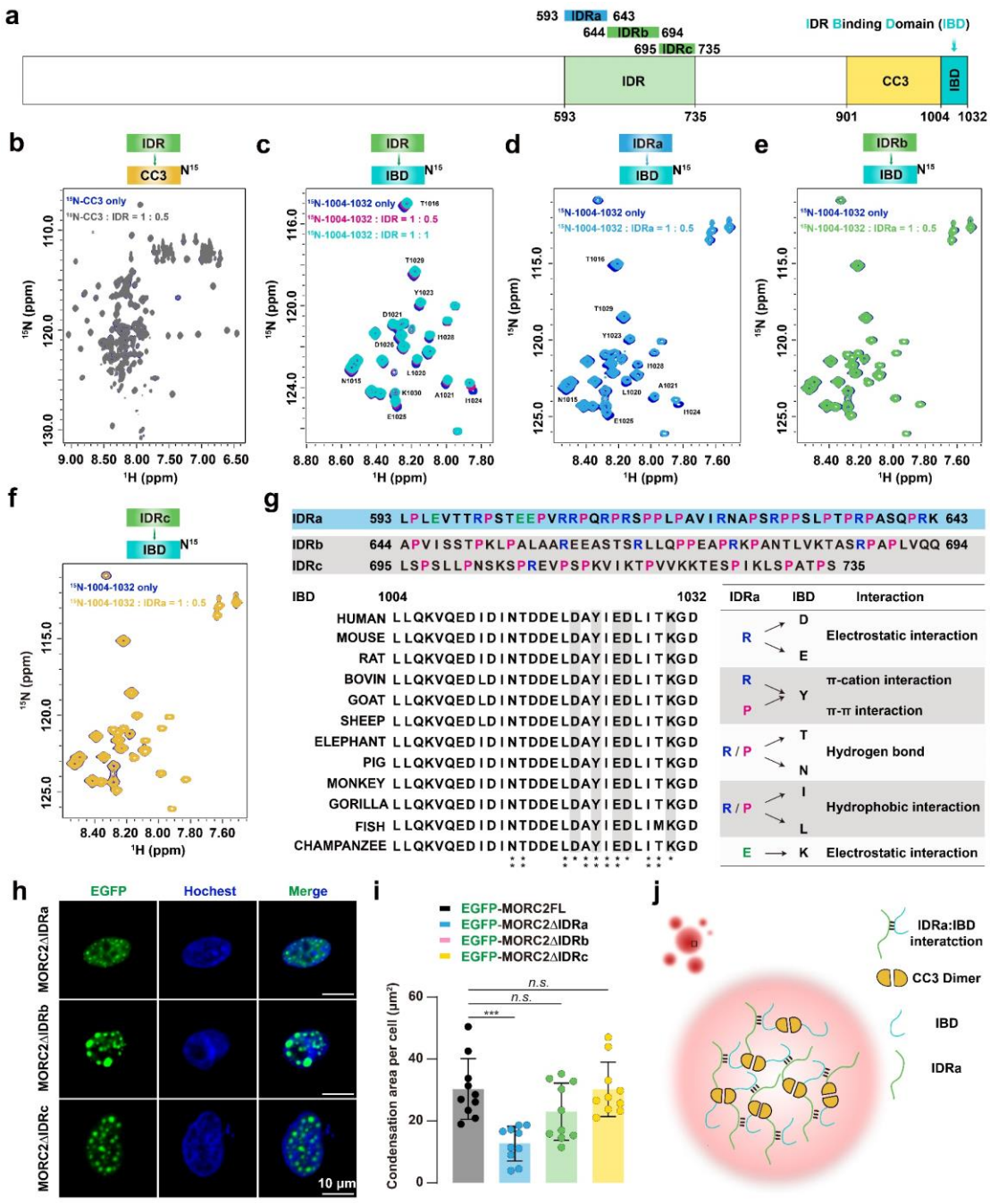
a
593 IDRa 643
644 IDRb 694
695 IDRc 735
IDR Binding Domain (IBD)
IDR
CC3
IBD
593
735
901
1004
1032
b
IDR
CC3
N15
15N-CC3 only
15N-CC3 : IDR = 1 : 0.5
15N (ppm)
1H (ppm)
c
IDR
IBD
N15
15N-1004-1032 only
15N-1004-1032 : IDR = 1 : 0.5
15N-1004-1032 : IDR = 1 : 1
d
IDRa
IBD
N15
15N-1004-1032 only
15N-1004-1032 : IDRa = 1 : 0.5
e
IDRb
IBD
N15
15N-1004-1032 only
15N-1004-1032 : IDRa = 1 : 0.5
f
IDRc
IBD
N15
15N-1004-1032 only
15N-1004-1032 : IDRa = 1 : 0.5
g
IDRa 593 LPLEVTTRPSTEEPVRRPQRPRSPPLPAVIRNAPSRPPSLPTPRPASQPRK 643
IDRb 644 APVISSTPKLPALAAREEASTSRLLQPPEAPRKPANTLVKTASRPAPLVQQ 694
IDRc 695 LSPSLLPNSKSPREVPSPKVIKTPVVKKTESPIKLSPATPS 735
IBD 1004 1032
HUMAN LLQKVQEDIDINTDDELDAYIEDLITKGD
MOUSE LLQKVQEDIDINTDDELDAYIEDLITKGD
RAT LLQKVQEDIDINTDDELDAYIEDLITKGD
BOVIN LLQKVQEDLDINTDDELDAYIEDLITKGD
GOAT LLQKVQEDLDINTDDELDAYIEDLITKGD
SHEEP LLQKVQEDLDINTDDELDAYIEDLITKGD
ELEPHANT LLQKVQEDIDINTDDELDAYIEDLITKGD
PIG LLQKVQEDIDINTDDELDAYIEDLITKGD
MONKEY LLQKVQEDIDINTDDELDAYIEDLITKGD
GORILLA LLQKVQEDIDINTDDELDAYIEDLITKGD
FISH LLQKVQEDIDINTDDELDAYIEDLIMKGD
CHAMPANZEE LLQKVQEDIDINTDDELDAYIEDLITKGD
IDRa IBD Interaction
R D E Electrostatic interaction
R Y π-cation interaction
P Y π-π interaction
R / P T N Hydrogen bond
R / P I L Hydrophobic interaction
E K Electrostatic interaction
h
EGFP
Hochest
Merge
MORC2ΔIDRa
MORC2ΔIDRb
MORC2ΔIDRc
10 μm
i
EGFP-MORC2FL
EGFP-MORC2ΔIDRa
EGFP-MORC2ΔIDRb
EGFP-MORC2ΔIDRc
n.s.
n.s.
***
Condensation area per cell (μm²)
j
IDRa:IBD interatction
CC3 Dimer
IBD
IDRa

Figure 4

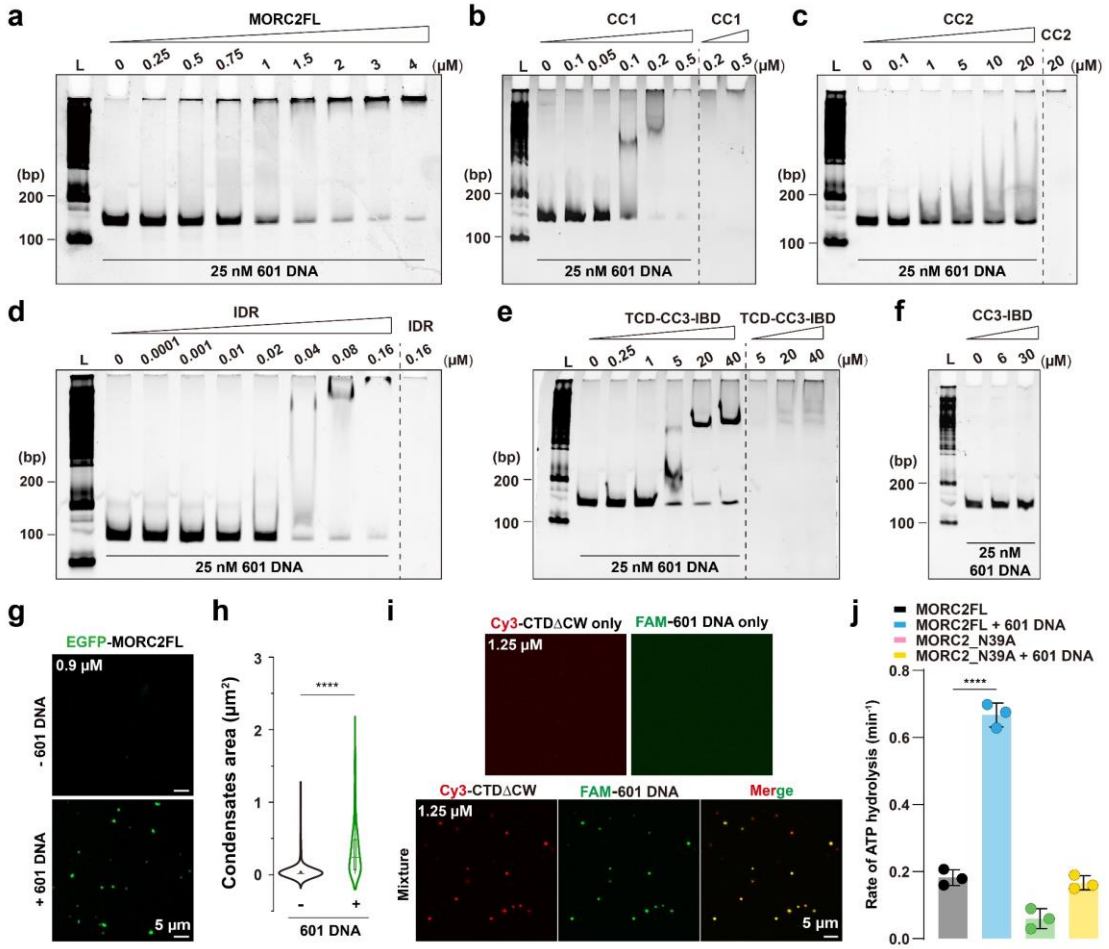
a
MORC2FL
L 0 0.25 0.5 0.75 1 1.5 2 3 4 (μM)
(bp)
200
100
25 nM 601 DNA
b
CC1
CC1
L 0 0.1 0.05 0.1 0.2 0.5 0.2 0.5 (μM)
25 nM 601 DNA
c
CC2
CC2
L 0 0.1 1 5 10 20 20 (μM)
25 nM 601 DNA
d
IDR
IDR
L 0 0.0001 0.001 0.01 0.02 0.04 0.08 0.16 0.16 (μM)
25 nM 601 DNA
e
TCD-CC3-IBD
TCD-CC3-IBD
L 0 0.25 1 5 20 40 5 20 40 (μM)
25 nM 601 DNA
f
CC3-IBD
L 0 6 30 (μM)
25 nM 601 DNA
g
EGFP-MORC2FL
0.9 μM
- 601 DNA
+ 601 DNA
5 μm
h
Condensates area (μm²)
****
601 DNA
i
Cy3-CTDΔCW only
FAM-601 DNA only
1.25 μM
Cy3-CTDΔCW
FAM-601 DNA
Merge
Mixture
1.25 μM
5 μm
j
MORC2FL
MORC2FL + 601 DNA
MORC2_N39A
MORC2_N39A + 601 DNA
Rate of ATP hydrolysis (min⁻¹)
****

Figure 5

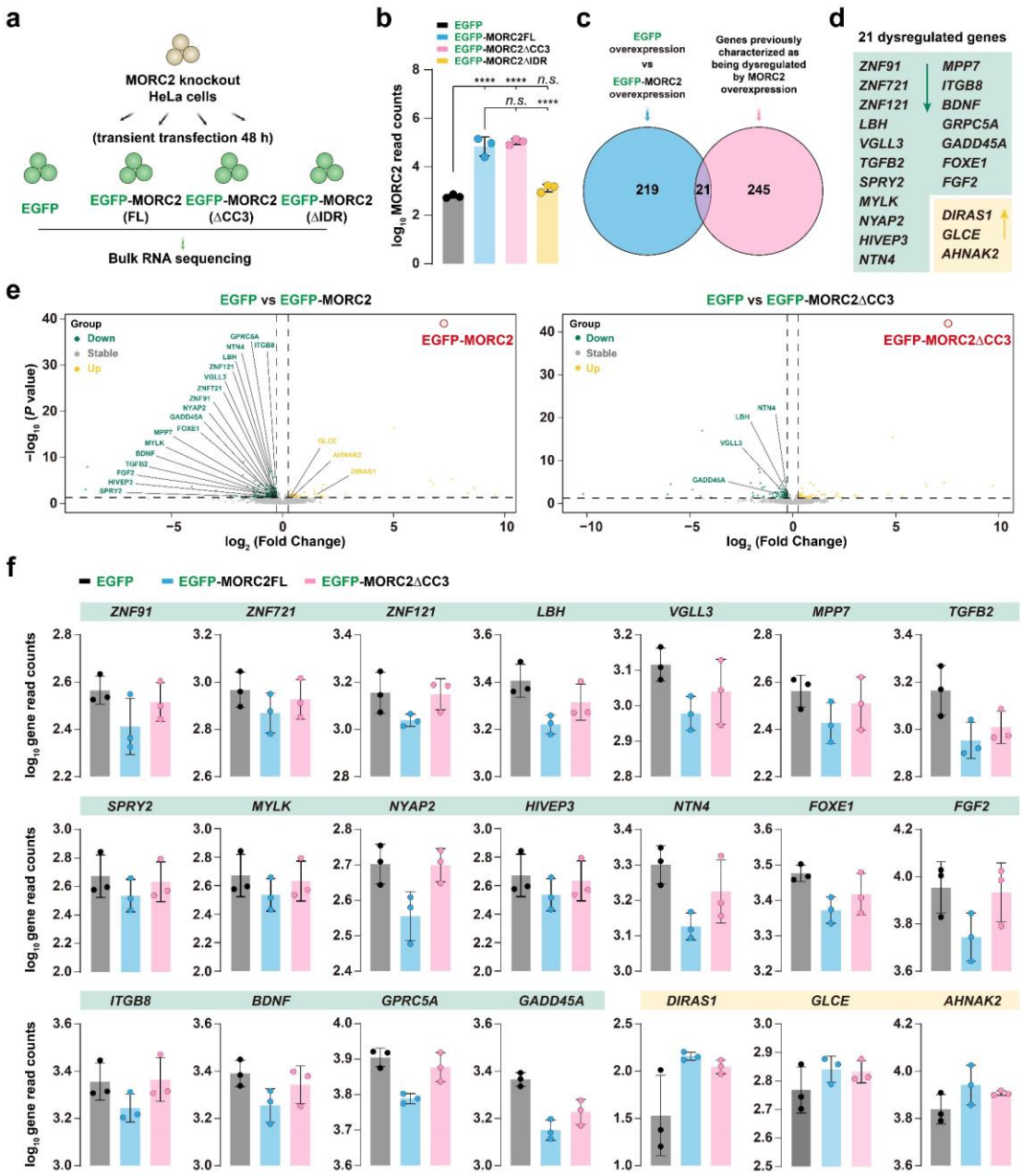
a
MORC2 knockout
HeLa cells
(transient transfection 48 h)
EGFP
EGFP-MORC2 (FL)
EGFP-MORC2 (ΔCC3)
EGFP-MORC2 (ΔIDR)
Bulk RNA sequencing
b
EGFP
EGFP-MORC2FL
EGFP-MORC2ΔCC3
EGFP-MORC2ΔIDR
log10 MORC2 read counts
****
n.s.
c
EGFP overexpression vs EGFP-MORC2 overexpression
Genes previously characterized as being dysregulated by MORC2 overexpression
219
21
245
d
21 dysregulated genes
ZNF91
ZNF721
ZNF121
LBH
VGLL3
TGFB2
SPRY2
MYLK
NYAP2
HIVEP3
NTN4
MPP7
ITGB8
BDNF
GRPC5A
GADD45A
FOXE1
FGF2
DIRAS1
GLCE
AHNAK2
e
EGFP vs EGFP-MORC2
EGFP vs EGFP-MORC2ΔCC3
Group
Down
Stable
Up
EGFP-MORC2
EGFP-MORC2ΔCC3
−log10 (P value)
log2 (Fold Change)
f
EGFP
EGFP-MORC2FL
EGFP-MORC2ΔCC3
log10 gene read counts
ZNF91
ZNF721
ZNF121
LBH
VGLL3
MPP7
TGFB2
SPRY2
MYLK
NYAP2
HIVEP3
NTN4
FOXE1
FGF2
ITGB8
BDNF
GPRC5A
GADD45A
DIRAS1
GLCE
AHNAK2

Figure 6

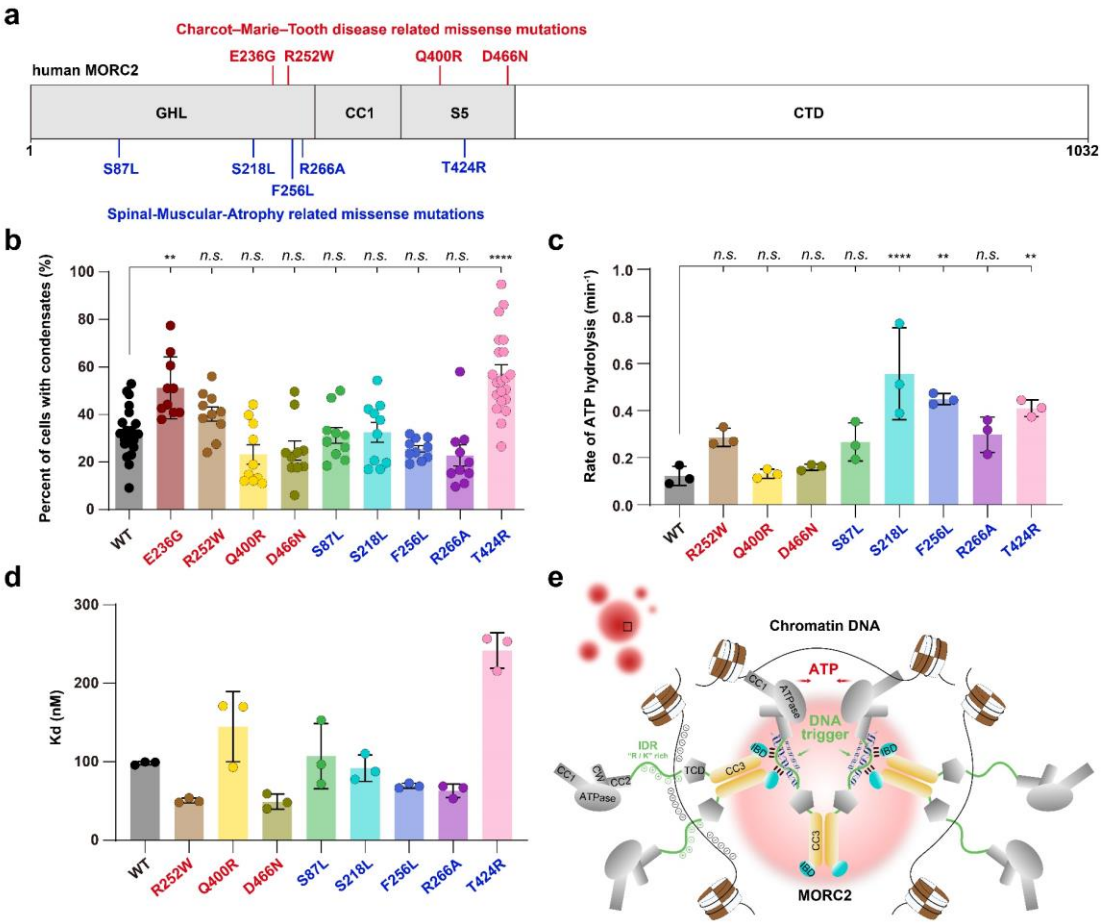
a
Charcot–Marie–Tooth disease related missense mutations
E236G R252W
Q400R D466N
human MORC2
GHL
CC1
S5
CTD
1
1032
S87L
S218L
R266A
F256L
T424R
Spinal-Muscular-Atrophy related missense mutations
b
Percent of cells with condensates (%)
WT
E236G
R252W
Q400R
D466N
S87L
S218L
F256L
R266A
T424R
c
Rate of ATP hydrolysis (min⁻¹)
d
Kd (nM)
e
Chromatin DNA
ATP
DNA trigger
IDR
CC1
ATPase
CC2
TCD
CC3
IBD
MORC2

Figure 7

Table S1

Statistics of X-ray Crystallographic Data Collection and Model refinement

Data collection	
Data sets	MORC2-CC3
Space group	*I41*
Wavelength (Å)	0.97915
Unit Cell Parameters (Å)	a=130.253, b=130.253, c= 40.895 α=β=γ=90°
Resolution range (Å)	50-3.05 (3.10-3.05)
No. of unique reflections	6774 (333)
Redundancy	12.6 (10.5)
I/σ	25.897 (2.600)
Completeness (%)	100.0 (100.0)
R_{merge} [a] (%)	12.0 (121.4)
$CC_{1/2}$ (last resolution shell) [b]	0.703
Structure refinement	
Resolution (Å)	32.56-3.10
R_{cryst} [c]/R_{free} [d] (%)	19.81 / 24.80
Rmsd bonds (Å) / angles (°)	0.004 / 0.627
Average B factor ($Å^2$) [e]	57.55
No. of atoms	
Protein atoms	1543
Water	6
Ligands	0
Ramachandran plot regions [e]	
Favored (%)	98.99
Allowed (%)	1.01
Outliers (%)	0

Numbers in parentheses represent the value for the highest resolution shell.

a. $R_{merge} = \Sigma\ |I_i - \langle I \rangle| / \Sigma I_i$, where I_i is the intensity of measured reflection and $\langle I \rangle$ is the mean intensity of all symmetry-related reflections.

b. $CC_{1/2}$ were defined by Karplus and Diederichs.

c. $R_{cryst}=\Sigma||F_{calc}| - |F_{obs}||/\Sigma F_{obs}$, where F_{obs} and F_{calc} are observed and calculated structure factors.

d. $R_{free}= \Sigma_T||F_{calc}| - |F_{obs}||/\Sigma F_{obs}$, where T is a test data set of about 5% of the total unique reflections randomly chosen and set aside prior to refinement.

e. B factors and Ramachandran plot statistics are calculated using MOLPROBITY.

Table S2. Summary of MORC2 protein constructs used in this study, including expression systems, extinction coefficients, A260/280 ratios, and corresponding experimental applications.

MORC2 fragment *in vitro*	**Expression system**	**Ext. coefficient**	**A260/280 ratios**	**Experimental applications**
MORC2FL (1-1032)	***E. coli***	88240	0.59	EMSA
CTD (473-1032)	*E. coli*	46410	0.71	EMSA; LLPS
CTDΔCW (537-1032)	*E. coli*	26930	0.58	EMSA; LLPS; FPLC-MALS
TCD-CC3-IBD (744-1032)	*E. coli*	26930	0.67	EMSA; FPLC-MALS
CC3-IBD (901-1032)	*E. coli*	7450	0.51	EMSA; FPLC-MALS
CC1 (279-362)	*E. coli*	1490	0.53	EMSA
CC2 (551-603)	*E. coli*	0	ND	EMSA
CC3 (901-1003)	*E. coli*	5960	0.49	FPLC-MALS NMR; Structure determination
IDR (593-735)	*E. coli*	0	ND	EMSA
IBD (1004-1032)	*E. coli*	1490	0.58	NMR
IDRa (593-643)	*E. coli*	0	ND	NMR
IDRb (644-694)	*E. coli*	0	ND	NMR
IDRc (695-735)	*E. coli*	0	ND	NMR
Trx-CC3	*E. coli*	21555	0.6	FPLC-MALS
Trx-CC3^{trun}_901-975	*E. coli*	14105	0.58	FPLC-MALS
Trx-CC3-IBD_L915Q	*E. coli*	21555	0.91	FPLC-MALS
Trx-CC3-IBD_F922Q	*E. coli*	21555	0.59	FPLC-MALS
Trx-CC3-IBD_L911Q	*E. coli*	21555	0.6	FPLC-MALS
Trx-CC3-IBD_I908Q	*E. coli*	21555	0.6	FPLC-MALS
Trx-CC3-IBD_F951Q	*E. coli*	21555	0.54	FPLC-MALS
Trx-CC3-IBD_Y921A	*E. coli*	20065	0.56	FPLC-MALS
Trx-CC3-IBD_F954Q	*E. coli*	21555	0.53	FPLC-MALS
Trx-CC3-IBD_L958Q	*E. coli*	21555	0.58	FPLC-MALS
MORC2FL (1-1032)	**HEK293F**	88240	0.6	FPLC-MALS; LLPS; FP; ATPase activity
MORC2ΔCC3-IBD (1-900)	HEK293F	80790	0.56	FPLC-MALS
MORC2_N39A	HEK293F	88240	0.79	FP; ATPase activity
MORC2_R252W	HEK293F	93740	0.66	FP; ATPase activity
MORC2_Q400R	HEK293F	88240	0.65	FP; ATPase activity
MORC2_D466N	HEK293F	88240	0.58	FP; ATPase activity
MORC2_S87L	HEK293F	88240	0.75	FP; ATPase activity
MORC2_S218L	HEK293F	88240	0.72	FP; ATPase activity
MORC2_F256L	HEK293F	88240	0.6	FP; ATPase activity
MORC2_R266A	HEK293F	88240	0.75	FP; ATPase activity
MORC2_T424R	HEK293F	88240	0.55	FP; ATPase activity
EGFP-MORC2FL	HEK293F	110130	0.59	LLPS; FRAP

Supplemental Figures

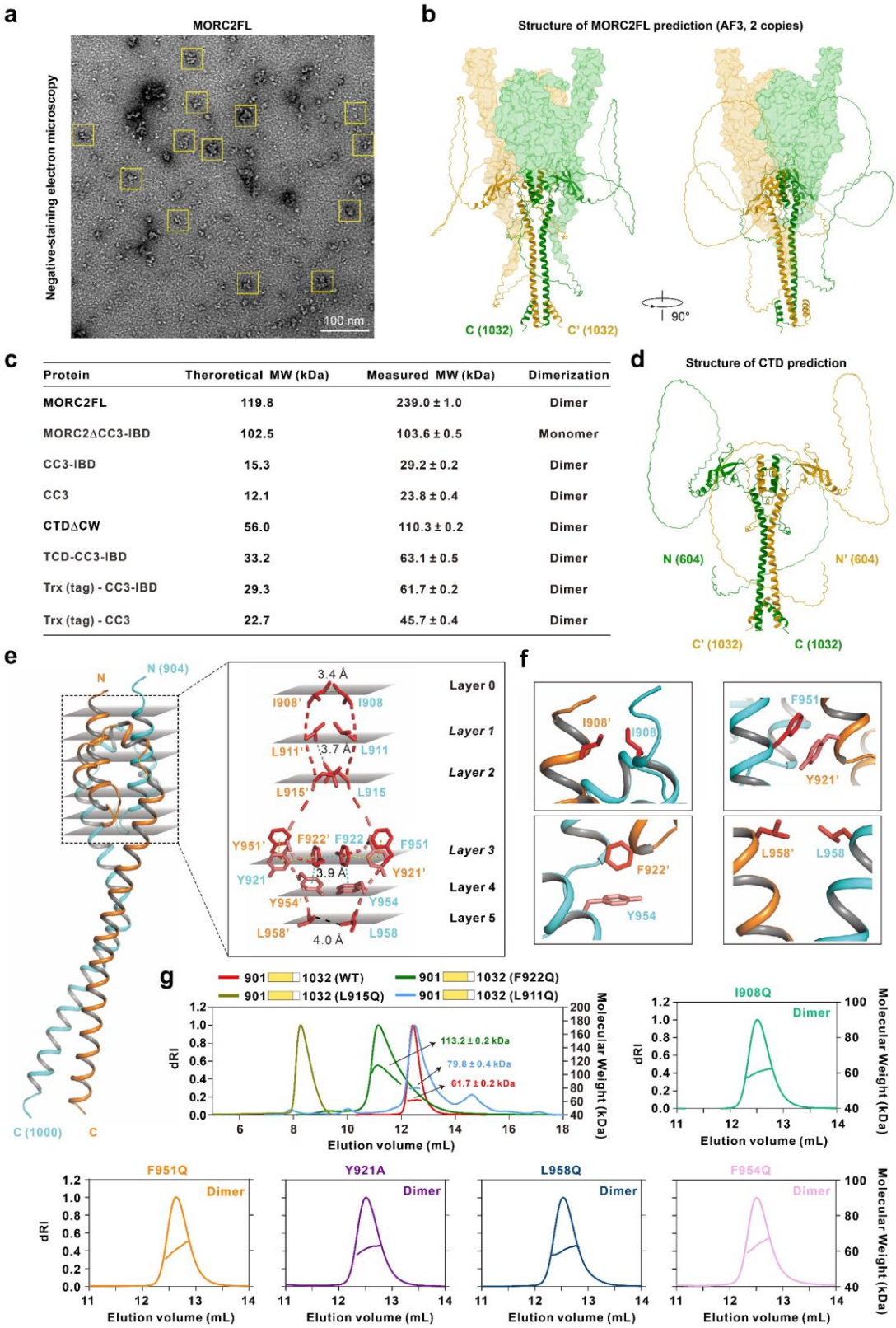

Protein	Theroretical MW (kDa)	Measured MW (kDa)	Dimerization
MORC2FL	119.8	239.0 ± 1.0	Dimer
MORC2ΔCC3-IBD	102.5	103.6 ± 0.5	Monomer
CC3-IBD	15.3	29.2 ± 0.2	Dimer
CC3	12.1	23.8 ± 0.4	Dimer
CTDΔCW	56.0	110.3 ± 0.2	Dimer
TCD-CC3-IBD	33.2	63.1 ± 0.5	Dimer
Trx (tag) - CC3-IBD	29.3	61.7 ± 0.2	Dimer
Trx (tag) - CC3	22.7	45.7 ± 0.4	Dimer

Fig. S1 Full-length MORC2 is a dimeric protein, with dimerization mediated by its C-terminal CC3 domain.

(a) Negative-stain electron microscopy revealed that MORC2FL particles purified from HEK293F cells appeared poorly resolved and exhibited considerable morphological heterogeneity. Scaler bar: 100 nm.

(b) Structural prediction of MORC2FL using AlphaFold3 under a two-copy modeling condition revealed the presence of an extended disordered region at the C-terminus and suggested a potential dimerization interface within this region.

(c) Summary of theoretical and measured molecular weight of MORC2 constructs, including MORC2FL, MORC2ΔCC3-IBD, CC3-IBD, CC3, and CC3 mutants. Data are derived from recombinant protein purification and static light-scattering (SLS) analysis.

(d) AlphaFold3-based modeling of MORC2 with the N-terminal domain removed revealed structural features of the C-terminus, including extensive disorder and a putative dimerization interface.

(e) Molecular model of the CC3 dimer highlights hydrophobic core residues (I908, L911, L915, F921, F922, F951, Y954). Key intermolecular distances include I908-I908’ (3.4 Å), L911-L915’ (3.7 Å), F922-F922’ (3.9 Å) and L958-L958’ (4.0 Å), supporting dimer stability.

(f) Molecular model of the CC3 dimer formation interface show the additional hydrophobic interactions.

(g) Point mutations in key residues (L911, L915, F922) affect dimerization. Additional mutants (I908Q, F951Q, Y921A, Y954A, L958Q) show no significant change in molecular weight compared to WT, confirming their minimal impact on dimer formation. SLS analysis shows molecular weight distributions, with WT CC3-IBD forming dimers (~ 60 kDa) as indicated by red curves, while mutants exhibit higher molecular weights indicative of aggregation. Constructs were tagged with a Trx tag (14 kDa) for solubility.

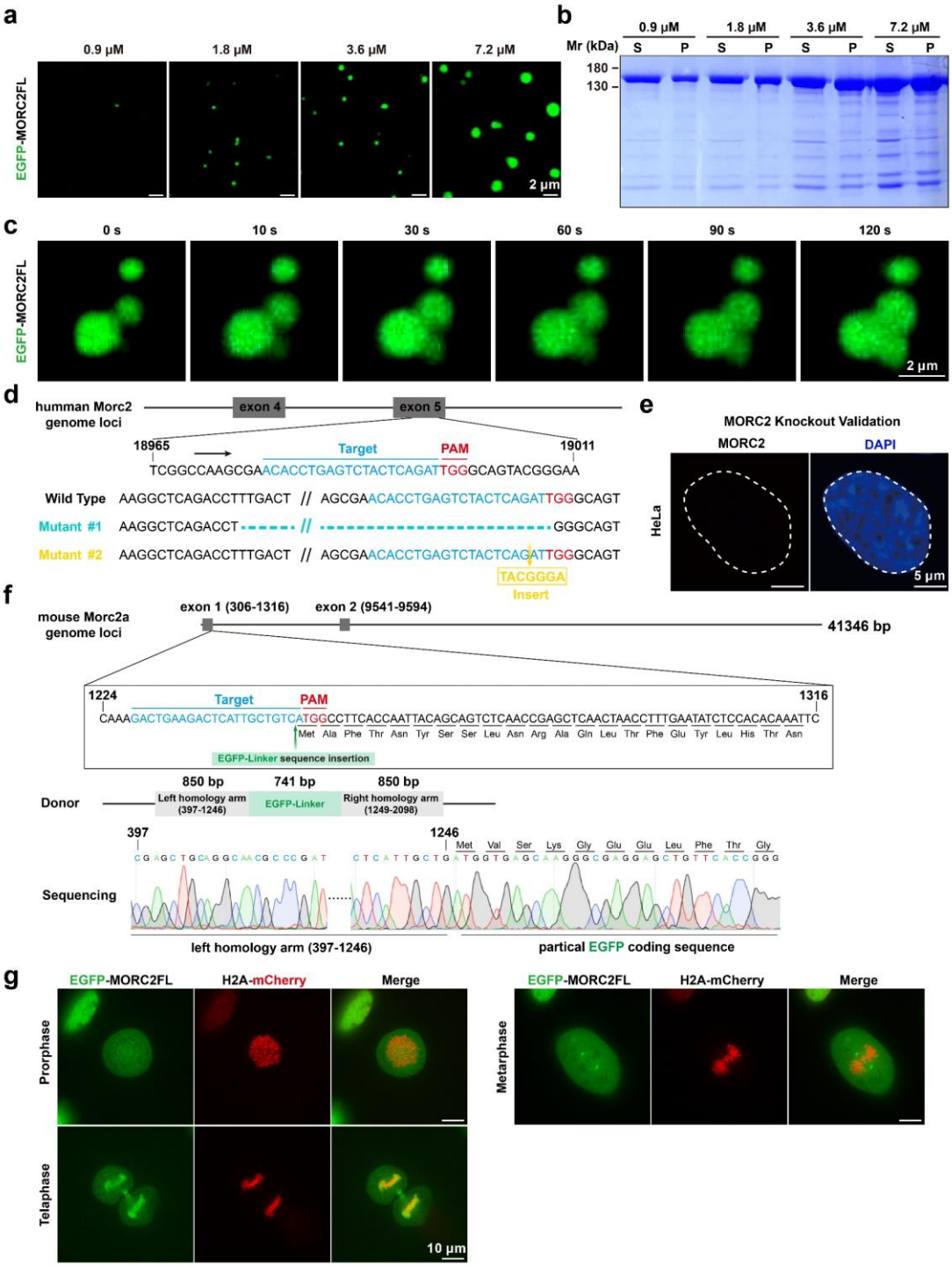

Fig. S2 *In vitro* and *in vivo* evidence that MORC2 undergoes LLPS.

(a) Concentration gradients of EGFP-MORC2FL proteins (0.9, 1.8, 3.6, and 7.2 μM) were analyzed for *in vitro* phase separation. The proteins were examined in a buffer containing 150 mM NaCl, and phase separation was characterized by fluorescence microscopy with 488 nm excitation for EGFP. Scaler bar: 2 μm.

(b) SDS-PAGE analysis of EGFP-MORC2FL in sedimentation-based assays. Protein

distribution between supernatant (S) and pellet (P) fractions is shown for increasing concentrations (0.9, 1.8, 3.6, and 7.2 μM).

(c) Time-lapse imaging of EGFP-MORC2FL phase separation over 120 s highlights dynamic droplet fusion. Scaler bar: 2 μm.

(d) Schematic of CRISPR-Cas9 strategy for generating MORC2 knockout (KO) HeLa cells. sgRNA targeting sequences and protospacer adjacent motifs (PAM) are highlighted. Genomic sequencing confirms insertion-deletion mutations introduced at target sites in MORC2 allelic genes.

(e) Immunostaining images of WT and MORC2 KO HeLa cells validate the specificity of the custom-made MORC2 antibody. Scaler bar: 5 μm.

(f) Generation of endogenous EGFP-MORC2 chimeric mice. Genomic sequencing confirms insertion-EGFP mutations introduced at target sites in MORC2 allelic genes.

(g) Live-cell imaging revealed that EGFP-MORC2FL exhibits dynamic subcellular localization throughout mitosis, without forming detectable condensates. Scaler bar: 10 μm.

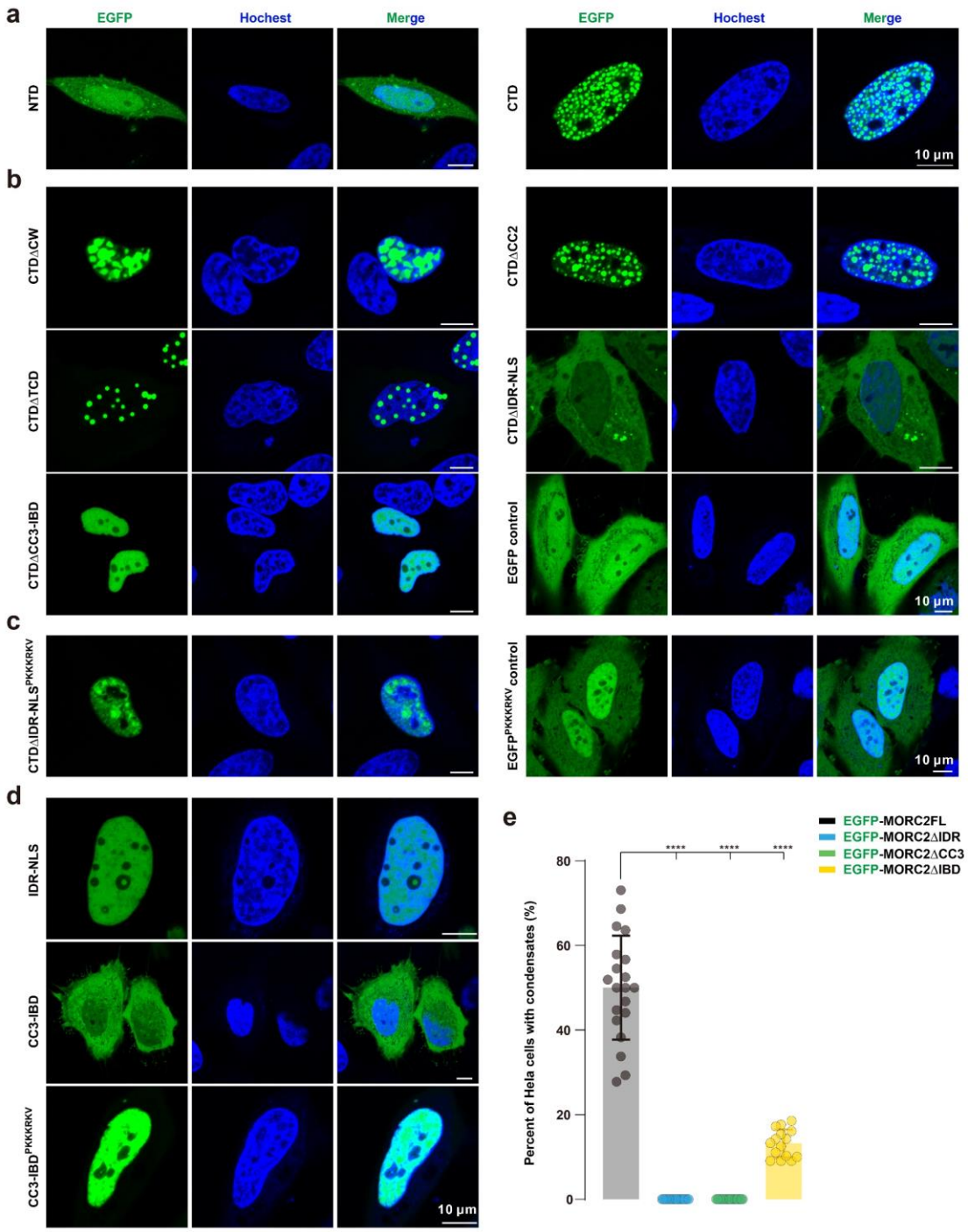

Fig. S3 The C-terminal domain (CTD) of MORC2 mediates nuclear condensate formation.

(a) EGFP-tagged MORC2 CTD forms nuclear condensates in HeLa cells, whereas the NTD does not. Scaler bar: 10 μm.

(b) Truncation analysis of EGFP-tagged CTD reveals that both the CC3-IBD and IDR-NLS regions are important for condensate formation. Scaler bar: 10 μm.

(c) EGFP-tagged CTD constructs lacking the IDR-NLS region but fused to an exogenous

N-terminal nuclear localization signal (“PKKKRKV”) successfully localize to the nucleus but fail to form condensates, indicating that the IDR is essential for phase separation. Scaler bar: 10 μm.

(d) Targeted expression of IDR-NLS and CC3-IBD fragments in the nucleus failed to induce condensate formation, indicating that these domains alone are not sufficient to drive phase separation. Scaler bar: 10 μm.

(e) The statistical data for droplet area in (Fig. 3a) demonstrate that the deletion of IDR or CC3 is imperative for condensate formation. The data are expressed as the mean ± standard error of the mean (SEM). $n \geq 15$ fields; one-way ANOVA with Tukey’s post hoc test. ****$P < 0.0001$.

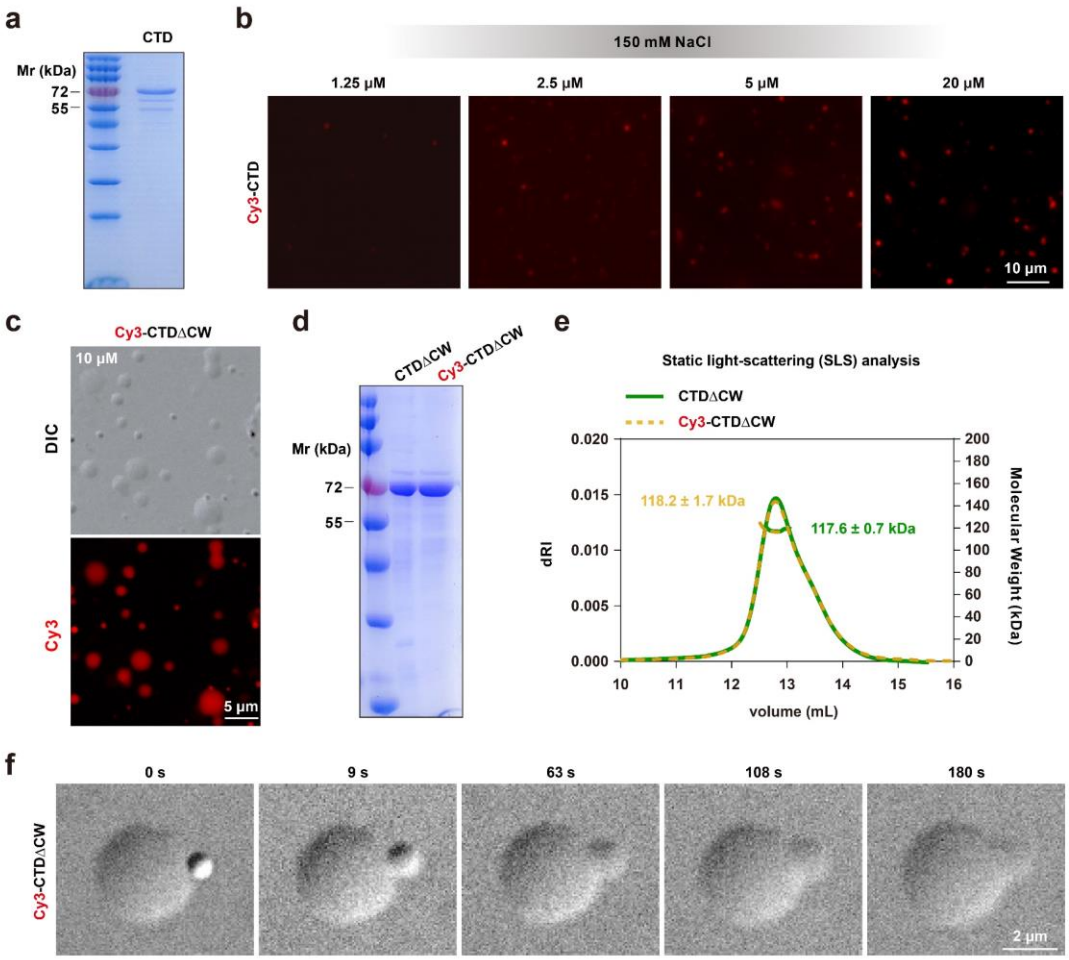

Fig. S4 The biophysical behavior of CTD and CTDΔCW *in vitro*.

(a) SDS-PAGE analysis of Cy3-labeled CTD showing expected size and degradative behavior.

(b) Fluorescence microscopy images of Cy3-labeledCTD at increasing protein concentrations (1.25 μM, 2.5 μM, 5 μM, and 10 μM) in standard phase separation buffer (50 mM Tris-Cl, pH 8.0, 150 mM NaCl). Despite increasing concentration, CW-CTD formed only small, dense puncta that did not exhibit robust size expansion or morphological changes. Scaler bar: 10 μm.

(c) Representative bright-field and Cy3 fluorescence microscopy images of labeled CTDΔCW protein droplets, showing intact condensate morphology under standard phase separation conditions. Scaler bar: 5 μm.

(d) SDS-PAGE analysis comparing Cy3-labeled and unlabeled CTDΔCW, indicating no degradation or mobility shift.

(e) Static light scattering (SLS) profiles of Cy3-labeled and unlabeled CTDΔCW

proteins reveal similar molecular weight distributions and hydrodynamic behavior.

(f) Time-lapse imaging of Cy3-labeled CTDΔCW over 180 s reveals dynamic droplet behavior *in vitro*. Scaler bar: 2 μm.

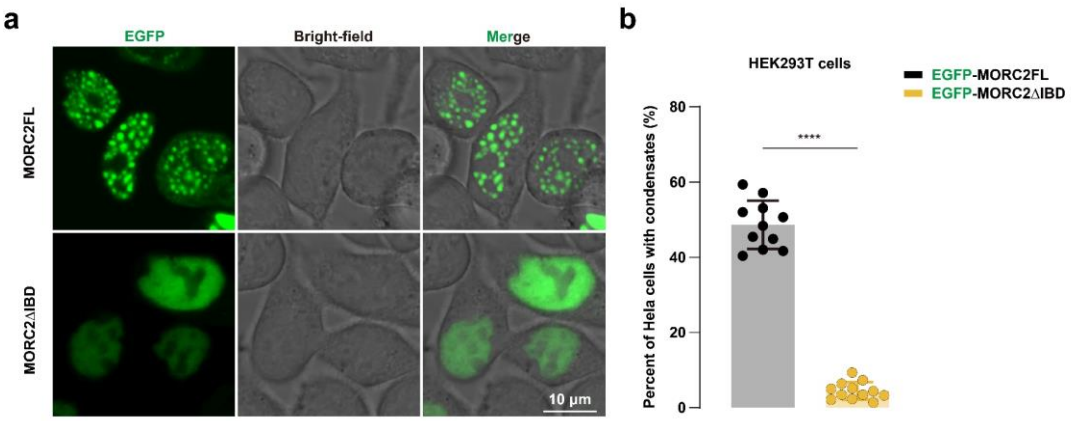

Fig. S5 Improved visualization of MORC2 nuclear condensates in HEK293T cells.

(a) Representative single-cell images of EGFP-MORC2-expressing HEK293T cells, reformatted from original Fig. 4i to enhance resolution and comparability with Fig. 4j. Nuclear puncta are clearly visible at this scale. Scaler bar: 10 μm.

(b) Quantification of the percentage of cells showing visible nuclear condensates in each construct. Data are presented as mean ± SEM; $n \geq 11$ replicates. Statistical significance was assessed using unpaired Student's *t*-test. ****$p < 0.0001$.

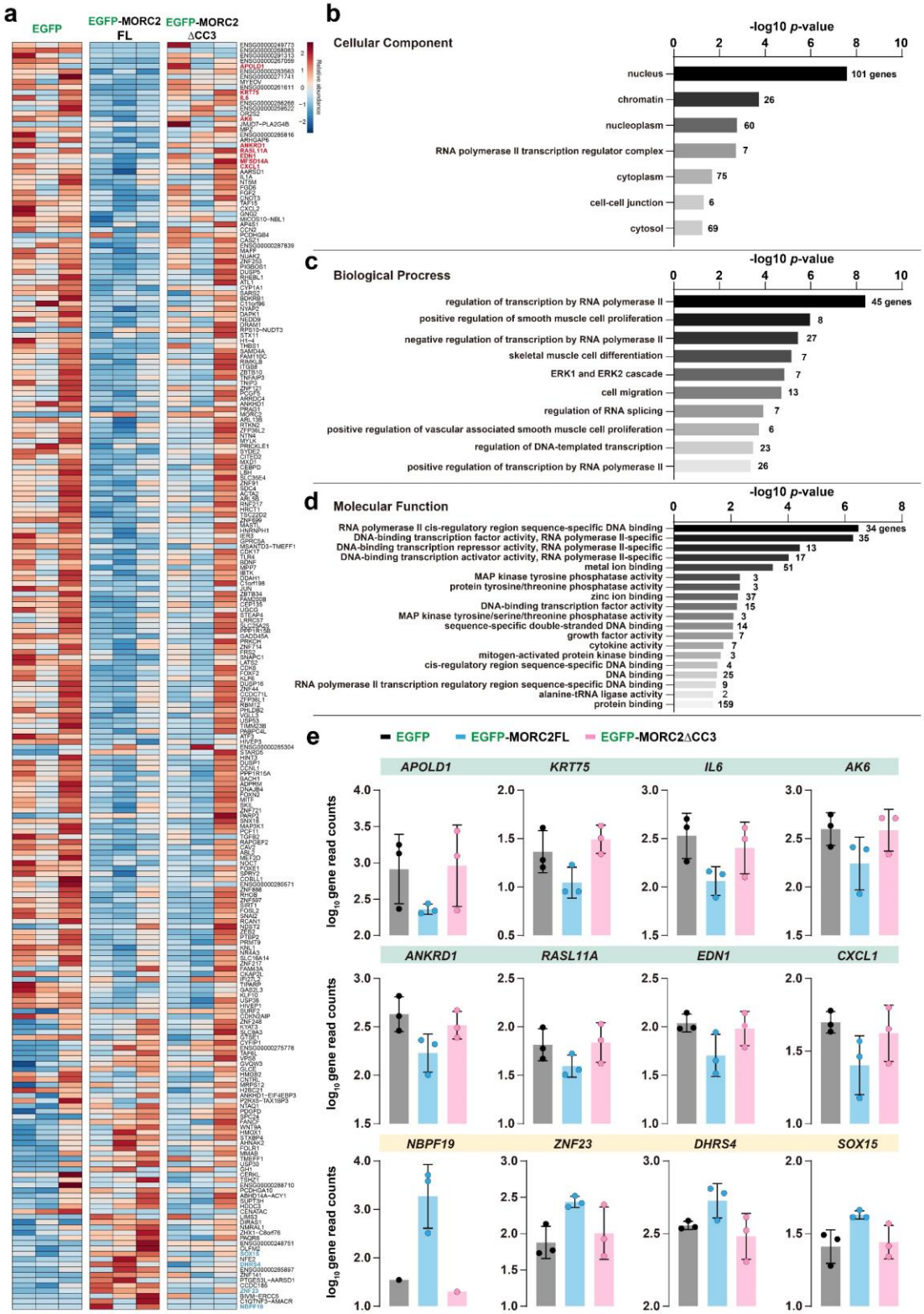

Fig. S6 MORC2 phase separation regulates gene transcription.

(a) Abundance trajectories of all 240 regulated genes were normalized to their respective mean values.

(b) GO-based cellular component analysis of the regulated genes mapped in DAVID

(v2025_1) knowledgebase. A substantial number of MORC2-regulated genes are primarily localized to the nucleus, chromatin, and nucleoplasm.

(c) GO-based biological process analysis. MORC2-regulated genes are predominantly involved in the biological process of transcriptional regulation.

(d) GO-based molecular function analysis. MORC2 primarily regulates genes encoding transcription factors with transcriptional regulatory activity. Additionally, MORC2 modulates the transcription of several cytokine genes.

(e) A selected panel of 12 genes that were regulated by MORC2 in this sequencing context but lost responsiveness to the LLPS-deficient mutant was shown, including 8 downregulated and 4 upregulated genes.

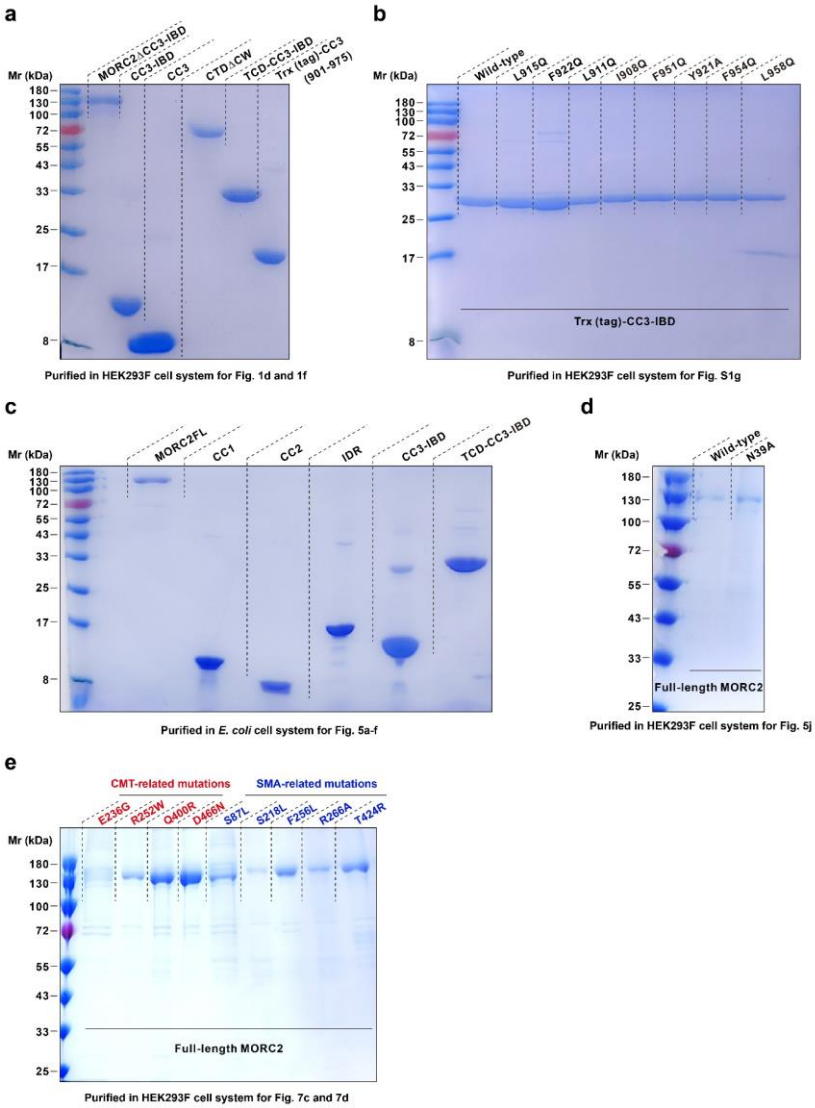

Fig. S7 Representative SDS-PAGE gels for all purified protein constructs.

(a) MORC2 fragments used for conformational analysis by FPLC-MALS (related to Fig. 1).

(b) MORC2 CC3 domain fragments used for dimerization analysis by FPLC-MALS (related to Fig. S1).

(c) MORC2 fragments expressed in *E. coli* for EMSA-based DNA-binding assays (related to Fig. 5).

(d) MORC2 fragments expressed in HEK293F cells for ATPase activity measurements with or without 601 DNA (related to Fig. 5).

(e) Disease-associated MORC2 mutants expressed in HEK293F cells for ATPase and DNA-binding assays,while E236G mutant exhibited poor biochemical properties, precluding further analysis *in vitro* (related to Fig. 7).